IJMMM International Journal of Minerals, Metallurgy and Materials 矿物冶金与材料学报（英文版）

# Kinetics of the hydrogen absorption and desorption processes of hydrogen storage alloys: A review

Qian Li, Xi Lin, Qun Luo, Yuan Chen, Jingfeng Wang, Bin Jiang, and Fusheng Pan

Cite this article as:
Qian Li, Xi Lin, Qun Luo, Yuan Chen, Jingfeng Wang, Bin Jiang, and Fusheng Pan, Kinetics of the hydrogen absorption and desorption processes of hydrogen storage alloys: A review, *Int. J. Miner. Metall. Mater.*, 29(2022), No. 1, pp. 32-48. https://doi.org/10.1007/s12613-021-2337-8

View the article online at SpringerLink or IJMMM Webpage.

---

*International Journal of Minerals, Metallurgy and Materials*
*Volume 29, Number 1, January 2022, Page 32*
**https://doi.org/10.1007/s12613-021-2337-8**

**Invited Review**

# Kinetics of the hydrogen absorption and desorption processes of hydrogen storage alloys: A review

*Qian Li*[1,3),*,✉], *Xi Lin*[2),*], *Qun Luo*[3)], *Yu'an Chen*[1)], *Jingfeng Wang*[1)], *Bin Jiang*[1)], *and Fusheng Pan*[1)]

1) National Engineering Research Center for Magnesium Alloys, Chongqing University, Chongqing 400044, China
2) School of Materials Science and Engineering, Shanghai Jiao Tong University, Shanghai 200240, China
3) State Key Laboratory of Advanced Special Steels & Shanghai Key Laboratory of Advanced Ferrometallurgy & School of Materials Science and Engineering, Shanghai University, Shanghai 200444, China
(Received: 12 April 2021; revised: 3 August 2021; accepted: 5 August 2021)

**Abstract:** High hydrogen absorption and desorption rates are two significant index parameters for the applications of hydrogen storage tanks. The analysis of the hydrogen absorption and desorption behavior using the isothermal kinetic models is an efficient way to investigate the kinetic mechanism. Multitudinous kinetic models have been developed to describe the kinetic process. However, these kinetic models were deduced based on some assumptions and only appropriate for specific kinetic measurement methods and rate-controlling steps (RCSs), which sometimes lead to confusion during application. The kinetic analysis procedures using these kinetic models, as well as the key kinetic parameters, are unclear for many researchers who are unfamiliar with this field. These problems will prevent the kinetic models and their analysis methods from revealing the kinetic mechanism of hydrogen storage alloys. Thus, this review mainly focuses on the summarization of kinetic models based on different kinetic measurement methods and RCSs for the chemisorption, surface penetration, diffusion of hydrogen, nucleation and growth, and chemical reaction processes. The analysis procedures of kinetic experimental data are expounded, as well as the effects of temperature, hydrogen pressure, and particle radius. The applications of the kinetic models for different hydrogen storage alloys are also introduced.

**Keywords:** hydrogen storage; metal hydrides; hydrogen absorption process; hydrogen desorption process; kinetic models

## 1. Introduction

Hydrogen storage is one of the key technologies to realize the applications of hydrogen energy, which can reduce environmental pollution and contribute to carbon neutrality. Hydrogen storage alloys (HSAs), such as $LaNi_5$, TiFe, $TiMn_2$, and $Mg_2Ni$, are a type of potential hydrogen storage material because of their high volumetric hydrogen density, high safety, and applicable working temperature and pressure [1−3]. HSA is usually employed as a material for hydrogen storage tanks (HSTs) used in specific applications, such as thermoelectric cogeneration systems [4] and fuel cell forklifts [5]. However, the low hydrogen charging and discharging rates of HST, which are caused by the heat of the hydriding/dehydriding reactions, are the main bottleneck for their applications [6−7]. The enhanced kinetics of the hydrogen absorption and desorption reactions of HSA and the appropriate design of HST are two ways to improve the rate of HST. To enhance the kinetics of the hydrogen absorption and desorption reactions of HSA, it needs to be modified based on an in-depth understanding of its kinetic mechanism. The HST can be designed effectively using numerical simulation. In the mathematical model, the kinetic equation is a key governing equation and determines the accuracy of the simulation [6]. Thus, how to analyze the kinetic mechanism of the hydrogen absorption and desorption processes of HSA is a core topic for the applications of hydrogen energy.

Generally, the reactions can be mainly classified into the solid–solid, gas–solid, and liquid–solid reactions [8−12]. The hydriding/dehydriding reactions are typical gas–solid reactions. The kinetic mechanism of the hydriding/dehydriding reactions can be determined through the analysis of the hydrogen absorption and desorption behavior using the isothermal kinetic models. Both external factors (temperature and pressure) and internal factors (elementary composition, particle radius, particle surface states, and hydrogen diffusion coefficient) can influence the kinetic process of hydrogenation/dehydrogenation [13]. Numerous isothermal kinetic models, such as the Jander [14−19], Chou [20−26], and Johnson–Mehl–Avrami–Kolmogorov (JMAK) [27−32] models, have been proposed and extensively applied in the investigation of hydrogenation/dehydrogenation. The effects of the external factors are expressed in the kinetic models as the activation energy and pressure terms. By contrast, the effects of the internal factors, except for the particle radius, are difficult to express in the kinetic models explicitly. Thus, the rate

* These authors contributed equally to this work.
✉ Corresponding author: Qian Li E-mail: cquliqian@cqu.edu.cn

constant is always used to represent the effects of the internal factors on hydrogenation and dehydrogenation in many kinetic models. Moreover, the volume expansion and contraction of particles during the hydrogen absorption and desorption processes could influence the prediction accuracy of the kinetic models for metal hydrides (MH) with large volume changes. However, some models rarely consider this factor. Thus, the appropriate kinetic model is indispensable to the analysis of the hydrogen absorption and desorption behavior.

Many processes exist objectively in the hydrogen absorption and desorption reactions of HSA. The hydrogen absorption and desorption processes can be generally divided into [12,33−35] (1) chemisorption, (2) surface penetration, (3) diffusion of hydrogen, (4) nucleation and growth, and (5) chemical reaction. However, the aforementioned isothermal kinetic models were deduced based on some assumptions and only appropriate for specific rate-controlling steps (RCS) and kinetic measurement methods. Thus, researchers without an in-depth understanding of kinetic models need the appropriate model to analyze experimental data. Many published reviews focused on the introduction of HSA [36−37] or its kinetic models [35,38] rather than the scope of application and kinetic analysis method according to the RCSs and kinetic measurement methods. Thus, we summarize the kinetic models according to different RCSs and kinetic measurement methods, as well as the progress of the development of new kinetic models.

This review mainly focuses on the isothermal kinetic models, kinetic parameters, and general analysis procedures of hydrogenation and dehydrogenation reactions. The framework of this review is shown in Fig. 1, as follows: (1) introducing the general isothermal kinetic model, including the model assumptions at different kinetic measurement methods and RCSs (Section 2); (2) summarizing the different analysis procedures of kinetic models, and the effects of temperature, pressure, and particle radius on the kinetics (Section 3); (3) illustrating the applications of the kinetic models for different types of HSA (Section 4).

## 2. General isothermal kinetic models

### 2.1. Hydrogen absorption and desorption processes

The general hydrogen absorption processes of metals or intermetallics are shown in Fig. 2. The hydrogen desorption of MH is the reverse process of hydrogen absorption. The hydrogen absorption processes can be described as follows: (a) The hydrogen molecules are physisorbed on the surface of the particle at a certain pressure. (b) The hydrogen molecules are dissociated to hydrogen atoms and chemisorbed on the surface of the metal (i.e., chemisorption). (c) The chemisorbed hydrogen atoms diffuse from the surface into the particle (i.e., surface penetration). (d) The MH nucleates and grows when the hydrogen concentration exceeds the solid solubility limit. Moreover, a chemical reaction occurs on the surface of MH in some HSAs with relatively low hydrogen solid solubility.

α represents the solid solution of hydrogen in alloys, which is formed first, as shown in Fig. 2(a). $r_0$ and $r$ are the radius of particle and unreacted core, respectively. When the diffusion rates of hydrogen atoms in the α phase are larger than the rates of chemisorption and surface penetration, the diffusion of hydrogen atoms in the α phase and physisorption are not regarded as the RCS. When the pressure of $H_2$ is higher than the MH equilibrium pressure, the phase transition of α → β can occur. First, the β layer will be generated on the surface of the particle. Then, the β layer will grow along the radial direction of the particle. Thus, hydrogen must diffuse through the β layer to the front of the phase transition of α → β (i.e., diffusion of hydrogen atoms in the β phase). If the nucleation and growth rates of β are slow, then there will be an α + β two-phase region between α and β (as shown in Fig. 2(b)). If the nucleation and growth rates of β are fast, then the α + β two-phase region will decrease until it can hardly be observed. Thereby, the phase transition of α → β can be simplified by a chemical reaction (as shown in Fig. 2(c)). The interface between α and β can be simplified as a continuously moving interface, which has been used as the assumption in many kinetic models, such as the Jander and Chou models.

The main hydrogen absorption and desorption measurement methods are the Sievert and flowing volumetric methods [39], as shown in Fig. 3. The Sievert method is the most common measurement technique [39], which can be easily implemented using the system of known volume when the temperature and pressure are measured accurately. The hydrogen absorption or desorption capacity can be calculated by the modified state equation of ideal gas using pressure change. In most cases, the initial pressure of the hydrogen volume is higher than the platform pressure of the α–β equilibrium. The β layer will be generated rapidly, and the state of the particle shown in Fig. 2(a) can be ignored. Thus, kinetic models, such as the Jander, JMAK, and Chou models [14], can be applied in most cases.

In the flowing volumetric method, the change of hydrogen amount in the sample cell is controlled by the mass flow controller (MFC), shown in Fig. 3(b) [39]. When the pressure and void volume of the sample cell are known, the hydrogen absorption or desorption capacity of HSA can be easily calculated. If the volume of the sample cell is small, then the capacity of HSA has an approximately linear relationship with time. When the pressure is less than the MH equilibrium pressure, the phase transition of α → β cannot occur. In this situation, the hydrogen absorption process may be controlled by two RCSs at different pressure ranges [6]. Because of the continuous pressure change, the experiment using the flowing volumetric method is regarded as a suitable way to reveal the kinetic mechanism of hydrogenation or dehydrogenation at different pressure ranges. However, only a few studies using the flowing volumetric method and the corresponding kinetic model have been published.

### 2.2. Kinetic models for the processes using the Sievert method

The kinetic models applied to the hydrogen absorption and desorption processes using the Sievert method, which include chemisorption, surface penetration, diffusion of hydro-

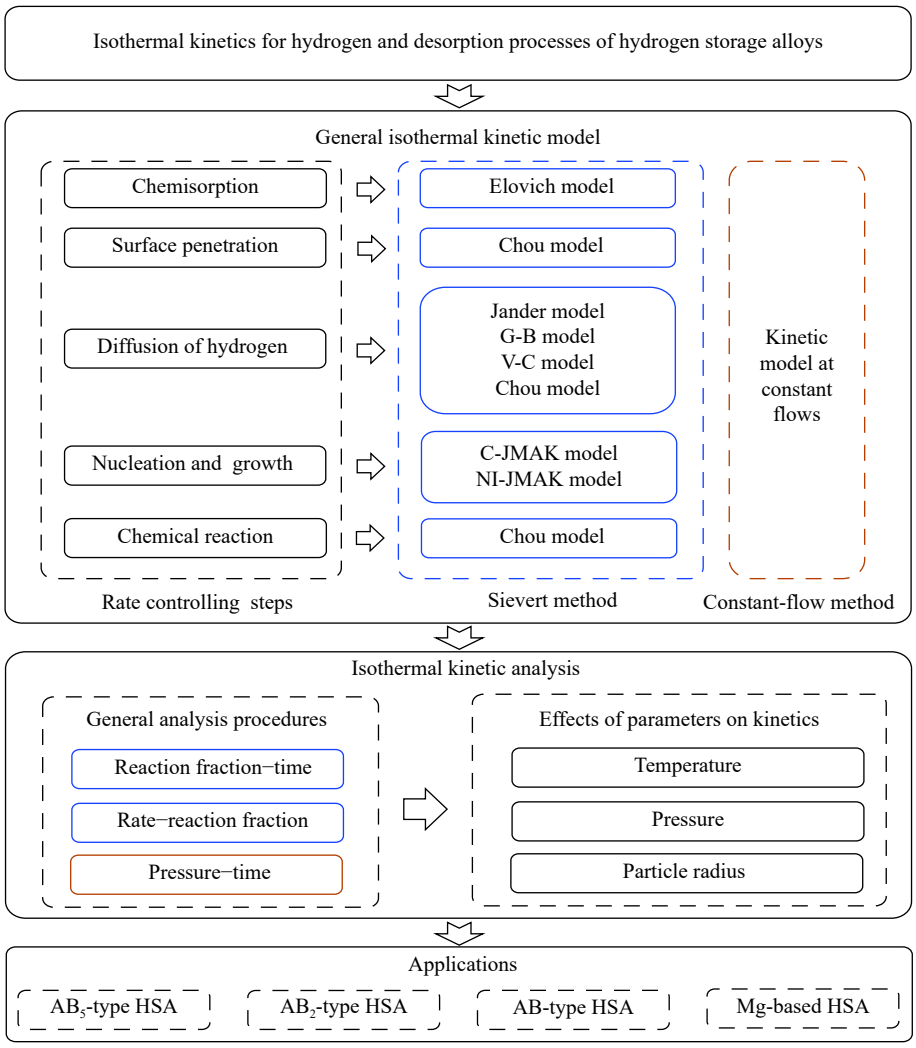


**Fig. 1. Framework diagram of this review.**

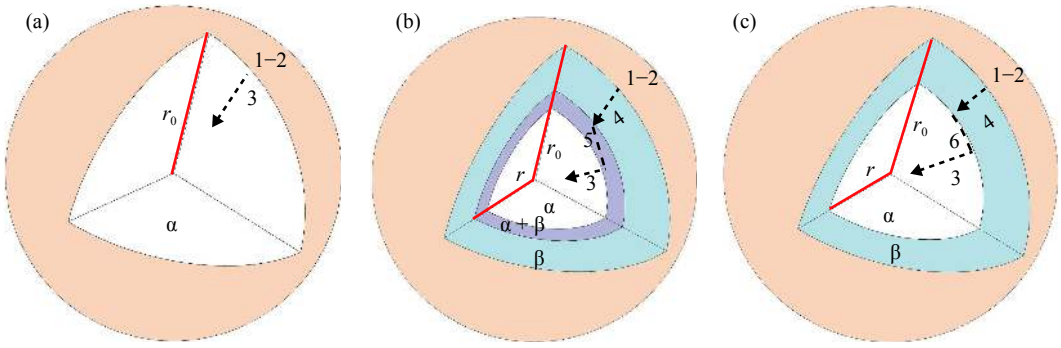


**Fig. 2. Schematic diagram of the hydrogen absorption processes of alloys: (a) without phase transition of α → β; (b) with α + β two-phase region; (c) without α + β two-phase region (continuously moving interface). 1—Chemisorption; 2—Surface penetration; 3—Diffusion of hydrogen in α phase; 4—Diffusion of hydrogen in β phase; 5—Nucleation and growth; 6—Chemical reaction.**

gen, nucleation and growth, and chemical reaction, are given in this review.

2.2.1. Chemisorption

The process of chemisorption can be expressed as follows:

$$H_2 + 2(\text{ch}) \leftrightarrow 2\text{H(ch)} \quad (1)$$

where (ch) is the empty site of chemisorption on the surface of the particle and H(ch) is the absorbed hydrogen. Generally, the process of chemisorption needs the activation energy $E$. With the increase of the percentage of the absorbed hydrogen on the particle surface ($\theta_{ch}$), the activation energy will increase, and the rate of chemisorption will decrease. The rate of chemisorption $v_{ch}$ can be calculated by the Elovich equation [40], as follows:

$$v_{ch} = k_{ch,0}^{ab} \exp\left(-\frac{E_{ch}^{ab} + a\theta_{ch}}{RT}\right)(1-\theta_{ch})^2 P + k_{ch,0}^{de} \exp\left(-\frac{E_{ch}^{de} + b\theta_{ch}}{RT}\right)\theta_{ch}^2 \quad (2)$$

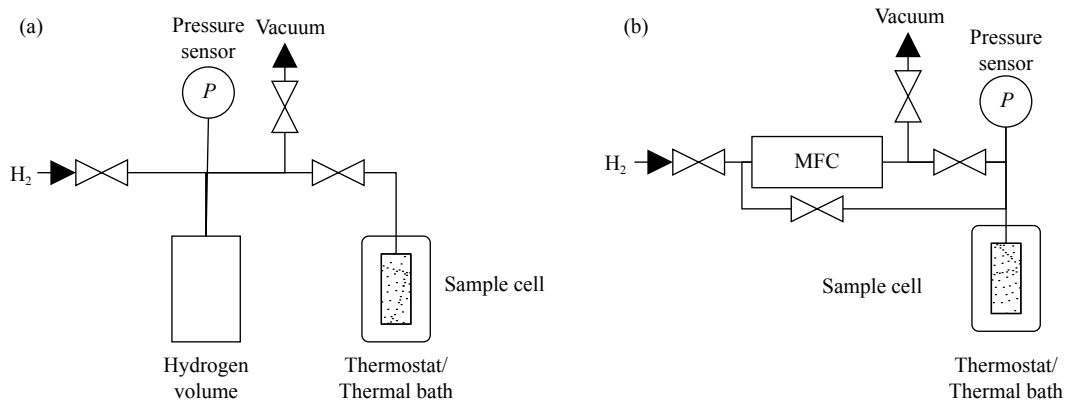


**Fig. 3. Schematic diagram of the hydrogen absorption and desorption measurement systems: (a) the Sievert method; (b) the flowing volumetric method.**

where $k_{ch,0}^{ab}$ and $k_{ch,0}^{de}$ are the rate constants of chemisorption for the hydrogen absorption and desorption processes, $R$ is the gas constant, $P$ is the pressure, $T$ is the temperature, $a$ and $b$ are the coefficients, and ab and de are the abbreviations of absorption and desorption, respectively. $\theta_{ch}$ is generally between 0 and 1. When $\theta_{ch}$ has a small value, the hydrogen desorption rate is low, and Eq. (2) can be simplified as follows:

$$v_{ch} = k_{ch,0}^{ab} \exp\left(-\frac{E_{ch}^{ab} + a\theta_{ch}}{RT}\right)P \tag{3}$$

When $\theta_{ch}$ has a medium value, Eq. (2) can be simplified as follows:

$$v_{ch} = k_{ch,0}^{ab} \exp\left(-\frac{E_{ch}^{ab} + a\theta_{ch}}{RT}\right)P + k_{ch,0}^{de} \exp\left(-\frac{E_{ch}^{de} + b\theta_{ch}}{RT}\right) \tag{4}$$

Aside from the Elovich equation, the chemisorption rate can be expressed as follows [12]:

$$v_{ch} = \frac{k_{ch}}{r_0}(P - P_{eq}) \tag{5}$$

where $r_0$ is the initial particle radius, $P_{eq}$ is the MH equilibrium pressure, $k_{ch}$ is the rate constant of chemisorption. In Eq. (5), the effects of particle radius and equilibrium pressure on the chemisorption rate are considered. Then, combined with the Arrhenius equation, Eq. (5) can be expressed as [12]

$$\xi = \frac{k_{ch,0}}{r_0} \exp\left(-\frac{E}{RT}\right)(P - P_{eq})t \tag{6}$$

where $\xi$ is the reaction fraction and $t$ is the time, $k_{ch,0}$ is the factor for the rate constant of chemisorption.

2.2.2. Surface penetration

The process of surface penetration can be expressed as follows:

$$H(ch) \leftrightarrow [H] + (ch) \tag{7}$$

where [H] is hydrogen in the α or β phase. The rate of surface penetration $v_{sp}$ can be expressed as follows [12,33]:

$$v_{sp} = k_{sp}^{ab}\theta_{ch} - k_{sp}^{de}C_{\beta} \tag{8}$$

where $k_{sp,0}^{ab}$ and $k_{sp,0}^{de}$ are the rate constants of surface penetration for the hydrogen absorption and desorption processes, and $C_{\beta}$ is the hydrogen concentration in β phase. When surface penetration is the RCS, other steps of the hydrogen absorption or desorption process can reach a quasi-equilibrium state. Thus, the rate of surface penetration can be expressed as follows [12,33]:

$$v_{sp} = \frac{k_{sp}}{r_0}(P^{1/2} - P_{eq}^{1/2}) \tag{9}$$

where $k_{sp}$ is the rate constants of surface penetration. Then, Eq. (9) can be changed to the form of reaction fraction with time, as follows:

$$\xi = \frac{k_{sp,0}}{r_0} \exp\left(-\frac{E}{RT}\right)(P^{1/2} - P_{eq}^{1/2})t \tag{10}$$

where $k_{sp,0}$ is the factor for the rate constant of surface penetration.

For the RCSs of chemisorption and surface penetration, the reaction fraction has a linear relationship with time. The main difference is the pressure term in the kinetic equations expressed in Eqs. (6) and (10). Thus, the effect of pressure on these two RCSs needs to be investigated.

2.2.3. Diffusion of hydrogen

Many kinetic models, such as the Jander [18], Ginstling–Brounshtein (G-B) [41], Valensi–Carter (V-C) [42], and Chou [33] models, have been used to describe the diffusion of hydrogen. These kinetic models are all derived based on the diffusion of hydrogen as RSC, with the temperature and pressure assumed to be constant during the hydrogen absorption and desorption processes.

(1) Jander model.

When the RCS is the diffusion of hydrogen, the reaction rate decreases proportionally with the thickness of the β layer. The Jander model assumes that the area of the α/β phase interface and the particle volume are constant [18,43]. Then, the moving rate of the α/β phase interface can be expressed based on Fick's law, as follows:

$$\frac{\rho \partial r}{\partial t} = -\frac{D\Delta C}{r_0 - r} \tag{11}$$

where $\rho$ is the density, $D$ is the diffusion coefficient, $\Delta C$ is the hydrogen concentration difference between the surface and the α/β phase interface, and $r$ is the radius of the α/β phase interface. The reaction fraction can be calculated by the following equation [44]:

$$\xi = 1 - \left(\frac{r}{r_0}\right)^d \tag{12}$$

where $d$ is the dimensionality. For spherical, cylindrical, and plate particles, $d$ is equal to 3, 2, and 1, respectively. Combining Eqs. (11) and (12), the Jander model can be expressed as follows:

$$[1-(1-\xi)^{1/d}]^2 = \frac{2D\Delta C}{r_0^2}t = k_{di}t \tag{13}$$

where $k_{di}$ is the rate constant of hydrogen diffusion. The form of the Jander model is concise. However, as the area of the α/β phase interface changes with the hydrogen absorption and desorption reactions, a deviation between the Jander model and the actual situation is observed. Thus, the Jander model is applied to the hydrogen absorption and desorption processes of small particles because of the slight change of the area of the α/β phase interface in small particles.

(2) G-B model.

The G-B model is developed based on the Jander model without the assumption that the area of the α/β phase interface is constant [41,45]. For the cylindrical particle, the moving rate of the α/β phase interface can be derived as follows:

$$\frac{\rho\partial r}{\partial t} = -\frac{D\Delta C}{r\ln(r_0/r)} \tag{14}$$

For the spherical particle, the moving rate of the α/β phase interface can be derived as follows:

$$\frac{\rho\partial r}{\partial t} = -\frac{D\Delta C r_0}{(r_0-r)r} \tag{15}$$

Then, the G-B models for the cylindrical and spherical particles can be expressed as Eqs. (16) and (17), respectively:

$$(1-\xi)\ln(1-\xi)+\xi = \frac{4D\Delta C}{r_0^2\rho}t = k_{di}t \tag{16}$$

$$1-\frac{2}{3}\xi-(1-\xi)^{2/3} = \frac{2D\Delta C}{r_0^2\rho}t = k_{di}t \tag{17}$$

The G-B model is more complex than the Jander model, but it is more accurate than the Jander model because it considers the area variation of the α/β phase interface.

(3) V-C model.

The V-C model considers the volume variation of the spherical particle before and after the hydrogen absorption and desorption processes. Thus, Eq. (11) can be modified as follows [42]:

$$\frac{\rho\partial r}{\partial t} = -\frac{D\Delta C}{r - r^2/[zr_0^3 + r^3(1-z)]^{1/3}} \tag{18}$$

where $z$ is the volumetric expansion ratio. Then, the V-C model can be expressed as follows:

$$\frac{z-[1+(z-1)\xi]^{2/3}-(z-1)(1-\xi)^{2/3}}{z-1} = \frac{2D\Delta C}{r_0^2\rho}t = k_{di}t \tag{19}$$

Given the volume expansion and contraction of particles, the equation of the V-C model becomes complex. In most cases, the alloy particle is small because of pulverization during the activation procedures. The effect of the volume expansion and contraction of particles on the kinetic curve obtained using the V-C model is inapparent compared with that obtained using the Jander model.

(4) Chou model.

The Chou model focuses on the physical interpretation of the generalized rate constant $k_{di}$ [14,20–26,33,44]. The effect of temperature on $k_{di}$ is embodied by the Arrhenius equation. The effect of pressure is embodied by the pressure term, which indicates the chemical driving force. Then, $k_{di}$ can be expressed as follows:

$$k_{di} = \frac{k_{di,0}}{r_0^2}\exp\left(-\frac{E}{RT}\right)(P^{1/2}-P_{eq}^{1/2}) \tag{20}$$

where $k_{sp,0}$ is the factor for the rate constant of hydrogen diffusion. Similar to that of the Jander model, the equation of the Chou model for the RCS of the diffusion of hydrogen can be expressed as follows [33]:

$$[1-(1-\xi)^{1/d}]^2 = \frac{k_{di,0}}{r_0^2}\exp\left(-\frac{E}{RT}\right)(P^{1/2}-P_{eq}^{1/2})t \tag{21}$$

Further considering the volume expansion and contraction of different particles, Eq. (21) can be modified as follows [44]. For the spherical particle:

$$\int_0^\xi \frac{[z-(z-1)(1-\xi)]^{1/3}-(1-\xi)^{1/3}}{3(1-\xi)^{2/3}}\mathrm{d}\xi = \frac{k_{di,0}}{r_0^2}\exp\left(-\frac{E}{RT}\right)(P^{1/2}-P_{eq}^{1/2})t \tag{22}$$

For the cylindrical particle:

$$\int_0^\xi \left[\frac{z}{1-\xi}-(z-1)\right]^{1/2}\mathrm{d}\xi - \xi = \frac{k_{di,0}}{r_0^2}\exp\left(-\frac{E}{RT}\right)(P^{1/2}-P_{eq}^{1/2})t \tag{23}$$

For the plate particle:

$$\xi^2 = \frac{k_{di,0}}{r_0^2}\exp\left(-\frac{E}{RT}\right)(P^{1/2}-P_{eq}^{1/2})t \tag{24}$$

The Chou model describes the functional relationship between rate and temperature, pressure, particle radius, and equilibrium pressure. Moreover, the Chou model proposes the concept of "characteristic time $t_c$," whose value is equal to $1/k_{di}$, to describe the time required for hydrogen absorption and desorption reactions to reach a specific reaction fraction (such as 100%, 80%, or 50%) [33].

2.2.4. Nucleation and growth

Generally, the nucleation and growth processes can be described by the JMAK model.

(1) Classical JMAK (C-JMAK) model.

The well-known C-JMAK model can be expressed as follows [14,46–47]:

$$\xi = 1-\exp(-k_{ng}t^n) \tag{25}$$

where $n$ is the Avrami exponent, and $k_{ng}$ is the rate constant of nucleation and growth. Generally, the value of $n$ is equal to or greater than 0.5. Eq. (25) can be transformed into:

$$[-\ln(1-\xi)]^{1/n} = (k_{ng})^{1/n}t \tag{26}$$

or

$$\ln[-\ln(1-\xi)] = n\ln t + \ln k_{ng} \tag{27}$$

The RCS in the nucleation and growth processes may be the diffusion or movement of the interface [38]. Notably, this diffusion represents the diffusion of the hydrogen and metal atoms during the nucleation and growth processes. In Section 2.2.3, the diffusion of hydrogen indicates the long-range diffusion of the hydrogen atom in the β layer. The C-JMAK model has been widely applied to describe the hydrogen absorption and desorption processes of HSA because of its high practicality and the simplified form of its equation. In the C-JMAK model, the RCS should be evaluated based on the value of $n$. However, as the Avrami exponent $n$ is the fitting value, the RCS corresponding to $n$ should be further investigated for a specific hydrogen storage material (or refer to published works).

(2) Nucleation-index-incorporated JMAK (NI-JMAK) model.

The NI-JMAK model is developed from the C-JMAK model to consider the effect of the self-catalysis of the nucleation process [14,28]. The NI-JMAK model can be expressed as follows:

$$\xi = 1-\exp\left\{-k_{ng,0}^{c+d/m}\mathrm{Beta}\left(c,\frac{d}{m}+1\right)\exp\left(\frac{-cE_n-\frac{d}{m}E_g}{RT}\right)t^{c+d/m}\right\} \tag{28}$$

where $c$ is the nucleation index, $m$ is the growth mode parameter, $d/m$ is the growth index, $E_n$ is the activation energy of nucleation, and $E_g$ is the activation energy of growth. The NI-JMAK model utilizes five independent variables to describe the nucleation and growth processes under the isothermal condition. Because of the complicated form of the equation, its application to the hydrogen absorption and desorption processes of HSA is limited. However, the C-JMAK model is recommended as the fitting kinetic model for the RCS of nucleation and growth.

2.2.5. Chemical reaction

The chemical reaction process can be expressed as follows:

$$[\mathrm{H}](\alpha/\beta)+\mathrm{M}(\alpha/\beta)\leftrightarrow \mathrm{MH}(\alpha/\beta) \tag{29}$$

where [H](α/β), M(α/β), and MH(α/β) are the hydrogen, hydrogen storage, and metal hydride at the α/β phase interface, respectively. Many kinetic models, such as the contracting volume (CV) and Chou models, have been used to describe the chemical reaction process.

(1) CV model.

The chemical reaction process is simplified as the process of the movement of the α/β phase interface with a constant rate [48] and can be expressed as follows:

$$\frac{\partial r}{\partial t}=-k_{int} \tag{30}$$

where $k_{int}$ is the moving rate of the α/β phase interface. Combining Eqs. (12) and (30), the equation of the CV model can be expressed as follows:

$$1-(1-\xi)^{1/d}=\frac{k_{int}}{r_0}t=k_{cr}t \tag{31}$$

where $k_{cr}$ is the rate constant of chemical reaction.

(2) Chou model.

The equation of the Chou model for the RCS of the chemical reaction process can be expressed as follows [33]:

$$1-(1-\xi)^{1/d}=\frac{k_{cr,0}}{r_0}\exp\left(-\frac{E}{RT}\right)(P^{1/2}-P_{eq}^{1/2})t \tag{32}$$

where $k_{cr,0}$ is the factor for the rate constant of chemical reaction. The comparison between the CV and Chou models shows that the forms of their equations are similar. However, the Chou model expands the rate constant $k_{cr}$ into a function of temperature, particle radius, pressure, and equilibrium pressure, which endows the model with more physical significance.

Many kinetic models suitable for the processes using the Sievert method have been introduced in this section according to the difference in RCSs. Generally, all kinetic models should be applied to fit the experimental data tested by the Sievert method so that the RCS can be decided. However, to reduce the workload of researchers, the following suggestions are given: (1) When the hydrogen pressure is far from the hydrogen absorption or desorption platform pressure, the diffusion of hydrogen, nucleation and growth, and chemical reaction are likely to be the RCS. By contrast, when the hydrogen pressure is close to the hydrogen absorption or desorption platform pressure, chemisorption or surface penetration is likely to be the RCS. (2) For the HSA with a small particle radius and volumetric expansion ratio, the effect of the α/β phase interface area and the volume expansion and contraction of particles can be ignored. Thus, the Jander or Chou model is proposed for this type of HSA.

## 2.3. Kinetic models for the processes using the flowing volumetric method

Only a few studies focusing on kinetic models appropriated for the hydrogen absorption and desorption processes using the flowing volumetric method have been published. Lin *et al.* [6,49] employed a kinetic model at constant flow to analyze the hydrogen absorption and desorption processes of HSA using the flowing volumetric method. As the hydrogen flows are constants, the curve of reaction fraction with time is nearly linear when the hydrogen concentration is less than the maximum concentration of HSA. Thus, the curve of pressure with time is analyzed. Because of the continuous pressure curve, the effect of pressure on the kinetic process can be easily revealed.

The kinetic equation for the chemisorption process can be expressed as follows [6]:

$$P=\pm\frac{r_0F}{k_{ch,0}\exp(-\frac{E}{RT})}+P_{eq} \tag{33}$$

where $F$ is the flow per unit mass. "+" and "−" in "±" of Eq. (33) indicate the hydrogen absorption and desorption processes, respectively. $P_{eq}$ can be predicted by the Van't Hoff equation, as follows:

$$P_{eq}=f(\mathrm{H/M})\exp[-\frac{\Delta H}{R}(\frac{1}{T}-\frac{1}{T_{ref}})] \tag{34}$$

where H/M is the hydrogen concentration (defined as the

mole ratio of hydrogen and alloy), $T_{ref}$ is the reference temperature of the PCT curve, $f$(H/M) is the polynomial equation of the PCT curve at $T_{ref}$. The hydrogen in the void area of the sample cell can be ignored when the volume of the void area is small. Then, H/M can be calculated by the following equation:

$$\mathrm{H/M} = (\mathrm{H/M})_0 \pm \frac{2M_0}{V_m} Ft \tag{35}$$

where $V_m$ is the standard molar volume of gas, $M_0$ is the relative molar mass, and $(\mathrm{H/M})_0$ is the initial hydrogen concentration.

The kinetic equation for the surface penetration process can be expressed as follows [6]:

$$P = \left[ \pm \frac{r_0 F}{k_{sp,0} \exp(-\frac{E}{RT})} + \sqrt{P_{eq}} \right]^2 \tag{36}$$

The kinetic equation for the diffusion of hydrogen can be expressed as follows [6]:

$$P = \left\{ \frac{r_0^2 F[1-(1-\xi)^{1/3}]}{k_{di,0} \exp(-\frac{E}{RT})(1-\xi)^{1/3}} + \sqrt{P_{eq}} \right\}^2 \tag{37}$$

where $\xi$ can be calculated by the following equation:

$$\xi = \frac{\mathrm{H/M}}{\mathrm{H/M_{max}}} \tag{38}$$

where $\mathrm{H/M_{max}}$ is the maximum of H/M.

The kinetic equation for the nucleation and growth processes can be expressed as follows:

$$P = P_{eq} \exp\left[ \frac{\pm F}{k_{ng,0} \exp(-\frac{E}{RT}) n [-\ln(1-\xi)]^{\frac{n-1}{n}} (1-\xi)} \right] \tag{39}$$

The kinetic equation for the hydrogen absorption of the chemical reaction process can be expressed as follows:

$$P = \left[ \frac{r_0 F}{k_{cr,0} \exp(-\frac{E}{RT})(1-\xi)^{2/3}} + \sqrt{P_{eq}} \right]^2 \tag{40}$$

The kinetic equation for the hydrogen desorption of the chemical reaction process can be expressed as follows:

$$P = \left[ \frac{-r_0 F}{k_{cr,0} \exp(-\frac{E}{RT}) \xi^{2/3}} + \sqrt{P_{eq}} \right]^2 \tag{41}$$

Substituting Eqs. (34) and (35) into Eqs. (33), (36), (37), and (39) to (41), the equations of pressure with time at a constant flow are established for different processes. The form of the equation of the kinetic model at constant flow is complicated. The key to the kinetic model at constant flow is the accuracy of the prediction of $P_{eq}$.

## 3. Isothermal kinetic analysis

The kinetic models can be used to fit the experimental data of the hydrogen absorption and desorption reactions of HSA according to different kinetic measurement methods. The RCS of hydrogenation or dehydrogenation at different pressures, temperatures, and particle radii can be analyzed using the fitted results, as well as the values of activation energy and rate constant. In this section, the analysis of the experimental kinetic data is summarized.

### 3.1. General analysis procedures

According to the experimental data from different kinetic measurement methods, the analysis procedures have slight differences. For the Sievert method, the experimental data of reaction fraction with time, as well as the rate with reaction fraction, can be applied to analyze the kinetic mechanism. For the flowing volumetric method, the experimental data of pressure with time is applied. In this section, these analysis procedures are all summarized.

3.1.1. Plot of reaction fraction with time

The kinetic model can be used to analyze the experimental kinetic data of reaction fraction $\xi$ with time $t$. The hydrogen absorption and desorption processes of HSA are mostly controlled by chemisorption, surface permeation, diffusion of hydrogen, nucleation and growth, and chemical reaction. The general formula of the kinetic equation can be written as follows:

$$f(\xi) = kt \tag{42}$$

where $f(\xi)$ is the function of $\xi$ which depends on the type of RCS. The rate constant $k$ can be derived as follows:

$$k = k_0 \exp\left(-\frac{E}{RT}\right) h(r_0) g(P, P_{eq}) \tag{43}$$

where $h(r_0)$ and $g(P, P_{eq})$ are the influence terms of the particle radius and pressure, respectively, and $k_0$ is the factor of rate constant. The analysis procedures are shown in Fig. 4. According to the fitted results of the $f(\xi)$–$t$ curve using the kinetic models for different RCSs, the RCS and rate constant are determined. Then, repeating the fitting process using the $f(\xi)$–$t$ curves under different test conditions, including temperature, pressure, and particle radius, the activation energy $E$, $k_0$, $h(r_0)$, and $g(P, P_{eq})$ are all determined.

The RCS may change with the hydrogen concentration of

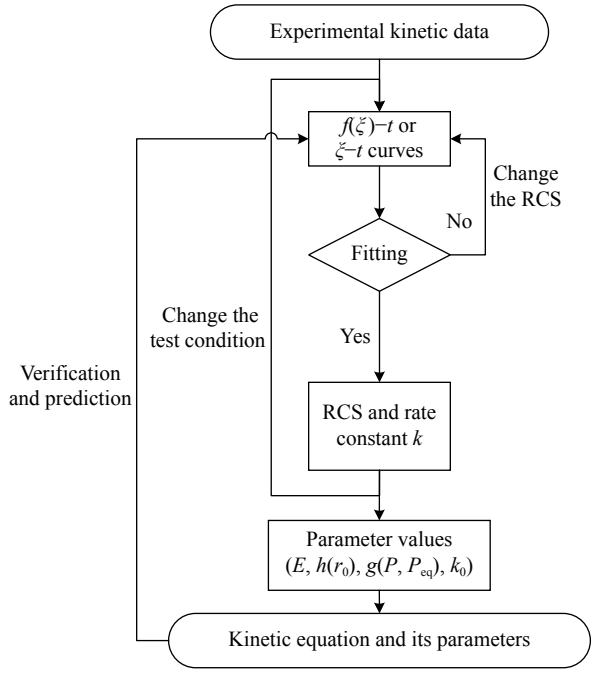


**Fig. 4. Kinetic analysis procedures for the plot of reaction fraction and time.**

some HSAs. Given the difference in $f(\xi)$ for different RCSs, the multistage fitted results cannot be easily presented in one plot of $f(\xi)$–$t$ visually. Thus, the plot of $\xi$–$t$ is used to analyze the kinetic process, as shown in Fig. 5. Most kinetic models can be transformed into the form of $\xi = f(t)$. A complete $\xi$–$t$ curve can be processed in three stages. The RCS of Stages 1 and 3 can be determined by the corresponding kinetic model. Stage 2 is the transitional stage, and its RCS is mixed. Its hydrogen absorption and desorption rate $v_2$ can be calculated by the following equation:

$$v_2 = \frac{1}{1/v_1 + 1/v_3} \tag{44}$$

where $v_1$ and $v_3$ are the hydrogen absorption and desorption rates of Stages 1 and 3, respectively.

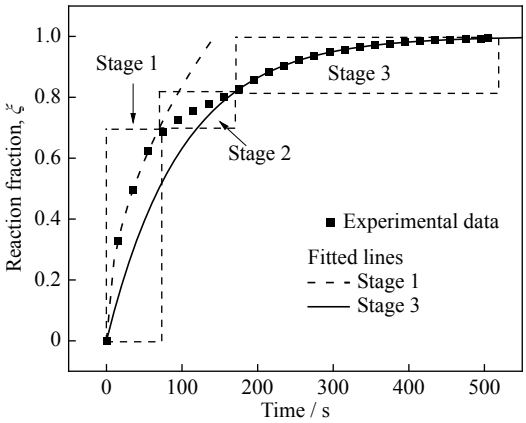


**Fig. 5. Schematic diagram of the plot of reaction fraction and time.**

3.1.2. Plot of rate and reaction fraction

The plot of rate and reaction fraction can also be used to analyze the kinetic process tested by the Sievert method [12,50]. When the particle of HSA is spherical, regardless of particle volume change, $\partial\xi/\partial t$ and $\xi$ can be plotted in Fig. 6 according to the kinetic models discussed in Section 2.2. For the chemisorption or surface penetration process, the rate does not change with the reaction fraction. Thus, the plot of $\partial\xi/\partial t$–$\xi$ is a straight line. For the diffusion of hydrogen, the rate decreases gradually with the increase of the reaction fraction. Thus, the plot of $\partial\xi/\partial t$–$\xi$ shows a semi-concave curve. For the nucleation and growth processes, the rate initially increases and subsequently decreases. Thus, the plot of $\partial\xi/\partial t$–$\xi$ shows a completely convex curve, which slightly differs with different $n$ values. For the chemical reaction process, the rate also decreases gradually with the increase of the reaction fraction. However, the plot of $\partial\xi/\partial t$–$\xi$ shows a semi-convex curve. The comparison between the experimental data and the $\partial\xi/\partial t$–$\xi$ curves plotted in Fig. 6 shows that the rate is controlled by the nucleation and growth processes ($n$ = 3) at $\xi < 0.2$, which then transform into the diffusion of hydrogen at $\xi > 0.2$. Thus, the plot of rate and reaction fraction can be applied to estimate the RCS at different reaction fraction ranges according to the line type.

3.1.3. Plot of pressure and time

The plot of pressure and time is used to analyze the kinetic process tested by the flowing volumetric method [6,49]. According to the kinetic model at constant flow discussed in Section 2.3, $P$ and $t$, as well as the fitted results, can be plotted in Fig. 7. The precondition for the application of this kinetic analysis method is the equilibrium pressure equation, which can be determined from the experimental PCT curves [51–54]. When the pressure is lower than or close to the MH equilibrium pressure, the β phase cannot be generated, and the potential RCS is chemisorption or surface penetration. When the pressure is higher than the MH equilibrium pressure, the β phase layer can be generated rapidly, and the potential RCS is the diffusion of hydrogen, nucleation and growth, or chemical reaction. Thus, according to the fitted result, the RCS can be determined at different pressure ranges.

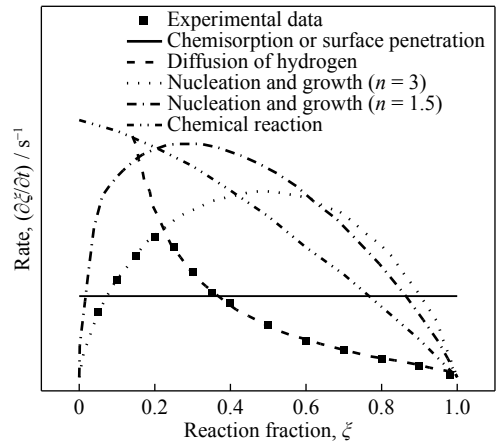


**Fig. 6. Schematic diagram of the plot of rate and reaction fraction.**

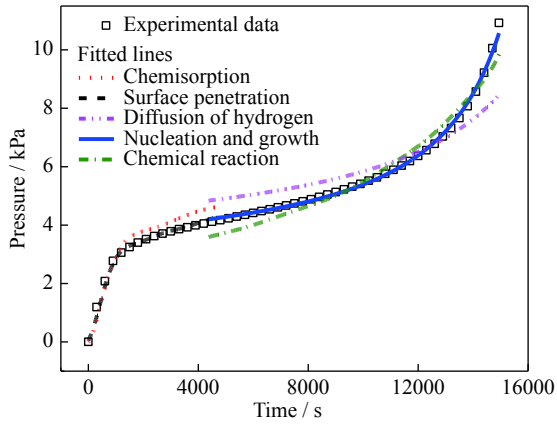


**Fig. 7. Schematic diagram of the plot of pressure and time.**

### 3.2. Effect of temperature on the hydrogen absorption and desorption kinetics

Given that the hydrogen absorption and desorption reactions of HSA are exothermic and endothermic processes, respectively, the temperature in the sample cell has a considerable effect on the reaction rate. The Arrhenius equation is a well-known equation used to embody the effect on the rate constant [55–56], which can be expressed as follows:

$$k = A\exp\left(-\frac{E}{RT}\right) \tag{45}$$

where $A$ is the pre-exponential factor. According to the fitted result of kinetic models, the values of rate constant $k$ at different temperatures can be determined. Then, plotting the curve of ln$k$ and $1/T$, the value of $E$ is evaluated. Table 1 shows the activation energy values of some typical HSAs. The activation energy values are compared in absorbed or desorbed one mol $H_2$ in this work. Generally, $k$ increases with temperature, and the value of $E$ is positive. However, as $k$ is related to the difference between pressure and equilibrium pressure, i.e., $g(P, P_{eq})$ term in Eq. (43), the value of $g(P, P_{eq})$ is considered to be close to the experimental data. Otherwise, the phenomenon that the value of $k$ decreases with temperature may occur.

### 3.3. Effect of hydrogen pressure on the hydrogen absorption and desorption kinetics

The driving force of the α → β phase transformation is the difference between hydrogen concentration and equilibrium hydrogen concentration, which is macroscopically represented by the difference between pressure and equilibrium pressure of HSA. Therefore, for the hydrogen absorption process, a high pressure leads to a fast hydrogen absorption rate. For the dehydrogenation process, a high pressure leads to a slow dehydrogenation rate. Notably, if the hydrogen absorption pressure is lower than the equilibrium pressure of α → β phase transformation, then only the hydrogen solid solution of the α phase will be generated. When the hydrogen absorption pressure is higher than the equilibrium pressure of the α → β phase transformation, the β phase layer will be generated on the surface of the particle rapidly. Therefore, the RCS will be different at different pressure ranges. The relationship between the rate constant and the pressure and equilibrium pressure can be expressed as follows:

$$k = k_0 g(P, P_{eq}) \tag{46}$$

In the Chou model, $g(P, P_{eq})$ is transformed into $P^{1/2} - P_{eq}^{1/2}$ directly. However, most kinetic models do not give the form of $g(P, P_{eq})$. Thus, the effect of pressure can be determined by kinetic experiments at different pressure ranges under the same temperature. Then, by plotting the curve of $k$ and $P$, the form of $g(P, P_{eq})$ can be evaluated based on the fitted results, such as $P$, $P^2$, $P$, $P_{eq}$, $(P - P_{eq})/P_{eq}$, and $\ln(P/P_{eq})$. Table 2 shows some forms of $g(P, P_{eq})$ for different HSAs. When determining the form of $g(P, P_{eq})$ using kinetic experiments, the RCS within the pressure range is generally required to remain consistent. Therefore, the form of $g(P, P_{eq})$ determined is generally only applicable to a specific pressure range. Notably, Eq. (46) cannot be applied to the kinetic models for the processes using the flowing volumetric method. The effect of pressure is included in pressure expansion.

### 3.4. Effect of particle radius on the hydrogen absorption and desorption kinetics

Generally, the specific surface area and diffusion cross section increase with the decrease of the particle radius

**Table 1. Activation energy and relevant RCSs for some HSAs**

| No. | HSA | Test conditions | RCS | $E$ / (kJ·mol$^{-1}$) | Ref. |
|---|---|---|---|---|---|
| 1 | $LaNi_5$ | 293–333 K, $P - P_{eq}$ = 100 kPa | Chemisorption | 19.66 (ab) | [57] |
| 2 | $LaNi_{4.5}Al_{0.5}$ | 273–343 K, $P - P_{eq}$ = 32.4 kPa | Chemisorption | 39.77 (ab) | [58] |
| 3 | $MmNi_{4.2}Al_{0.8}$ | 288–308 K, 0.013 MPa | Diffusion of hydrogen | 48.09 (de) | [59] |
| 4 | $La_{1.5}Ni_{0.5}Mg_{17}$ | 523–573 K, 0.755 MPa | Diffusion of hydrogen | 90 (ab) | [60] |
| 5 | ZrCo | 544–603 K, $P/P_0$ = 0.9–1 MPa | Nucleation and growth | 120 (ab) | [61] |
| 6 | TiFe | 243–298 K, 0.02 MPa | Chemisorption | 3.35 (ab) | [62] |
| 7 | $TiFe_{0.8}Ni_{0.2}$ | 373–423 K, $\lvert P_{eq} - P_{0.5}\rvert/P_{eq}$ [a] | Diffusion of hydrogen | 53.13 (ab) | [63] |
| 8 | $Zr_{0.2}Ho_{0.8}Co_2$ | 323–473 K, 0–5 MPa | — | 15 (ab) | [64] |
| 9 | $Ti_{33}V_{20}Cr_{47}$ | 293–353 K, 3.5 MPa | Diffusion of hydrogen | 25.7 (ab) | [65] |
| 10 | $Mg_2Ni$ | 528–623 K, 4 MPa | Diffusion of hydrogen | 44 (ab) | [22] |
| 11 | $Mg_{1.9}Ag_{0.1}Ni$ | 523–573 K, 0.768 MPa | Diffusion of hydrogen | 52 (ab) | [66] |
| 12 | $MgH_2$−5at%V | 453–573 K, 0.015 MPa | — | 62 (de) | [67] |

Note: [a] $P_{0.5}$ is the pressure at the reaction fraction of 0.5.

**Table 2. Some forms of $g(P, P_{eq})$ for different HSAs**

| No. | HSA | Test conditions | RCS | $g(P, P_{eq})$ | Ref. |
|---|---|---|---|---|---|
| 1 | $LaNi_5$ | $P - P_{eq}$ = 50−200 kPa, 303 K | Chemisorption | $P - P_{eq}$ | [57] |
| 2 | $LaNi_{4.5}Al_{0.5}$ | $P - P_{eq}$ = 25.3−66.9 kPa, 298 K | Chemisorption | $P - P_{eq}$ | [58] |
| 3 | $La_{1.5}Ni_{0.5}Mg_{17}$ | 0.256–0.992 MPa, 553 K | Diffusion of hydrogen | $[(P - P_{eq})/P_{eq}]^2$ | [60] |
| 4 | $Mg_2Ni$ | 0.275–1.133 MPa, 553 K | Diffusion of hydrogen | $P^{1/2} - P_{eq}^{1/2}$ | [22] |
| 5 | $MgH_2$−5at%V | 0.007–0.4 MPa, 533–673 K | — | $1 - P/P_{eq}$ | [68] |
| 6 | Mg−10wt%Ni | $P - P_{eq}$ = 20.1–54.6 kPa, 573 K | — | $[P - P_{eq}]^{1.25}$ | [69] |
| 7 | ZrCo | <1 MPa, 300 K | Chemisorption | $P^2$ | [70] |
| 8 | TiFe | 1.717–2.626 MPa, 294 K | Chemisorption | $P - P_{eq}$ | [62] |
| 9 | $TiFe_{0.8}Ni_{0.2}$ | 0.246–0.733 MPa, 408 K | — | $(P_{eq} - P)/P_{eq}$ | [71] |

[52,72−73]. Thus, decreasing the particle radius of HSA can enhance the hydrogen absorption and desorption rates. The relationship between rate constant and particle radius can be expressed as follows:

$$k = k_0 h(r_0) \tag{47}$$

For different hydrogen absorption and desorption processes, the influence of particle radius is also different: for physical adsorption, chemical adsorption, surface penetration, and chemical reaction, $h(r_0)$ is generally expressed as $1/r_0$; for the diffusion of hydrogen, $h(r_0)$ is generally expressed as $1/r_0^2$. Notably, no clear relationship between particle radius and rate constant of the nucleation and growth processes is observed, which generally needs to be evaluated by experiments.

## 4. Applications to the different types of HSA

The hydrogen absorption and desorption processes of HSA are complex and can be influenced by the preparation methods, powder particle state, and catalyst. Different kinds of HSA may have different RCSs; even the HSA with similar composition could have a different RCS. Notably, the kinetic model is semi-empirical. The completed hydrogen absorption and desorption kinetic mechanism should be further analyzed by conducting other experiments, such as scanning electron microscopy (SEM) and transmission electron microscopy (TEM) [74]. In this section, the kinetic studies of the hydrogen absorption and desorption processes of $AB_5$-type, $AB_2$-type, AB-type, and Mg-based HSAs are introduced.

### 4.1. $AB_5$-type HSAs

$LaNi_5$ is a typical $AB_5$-type HSA, and its hydrogen concentration curve at different pressure differences d$P$ of hydrogen absorption pressure and equilibrium pressure is shown in Fig. 8(a) [75]. The maximum hydrogen concentration increases with the increase of d$P$. Based on the CV model, the curves of $1-(1-\xi)^{1/3}$ and $t$ are plotted in Fig. 8(b). Notably, $1-(1-\xi)^{1/3}$ has a linear relationship with $t$, and the values of $R^2$ are higher than 0.98. The fitted slopes are the value of the rate constant. Thus, the RCS for the hydrogen absorption process of $LaNi_5$ is the chemical reaction. With the decrease of d$P$ from 200 to 50 kPa, the rate constants $k_{cr}$ are 0.01457, 0.00768, and 0.00461 $s^{-1}$. The equilibrium pressure $P_{eq}$ of the alloy at 323 K is approximately 530 kPa. Assuming that the form of $g(P, P_{eq})$ in Eq. (43) is $\ln(P/P_{eq})$, the curve of $k_{cr}$ and $\ln(P/P_{eq})$ can be plotted in Fig. 8(c). The linear fitted result of $k_{cr}$ and $\ln(P/P_{eq})$ indicates that the form of $g(P, P_{eq})$ in Eq. (43) can be evaluated as $\ln(P/P_{eq})$. Thus, the kinetic equation of $LaNi_5$ can be written as follows:

$$1-(1-\xi)^{1/3} = k'_{cr}\ln(P/P_{eq})t = k_{cr,0}\exp\left(-\frac{E}{RT}\right)\ln(P/P_{eq})t \tag{48}$$

where $k'_{cr}$ is a coefficient.

Then, according to the experimental kinetic curves at dif-

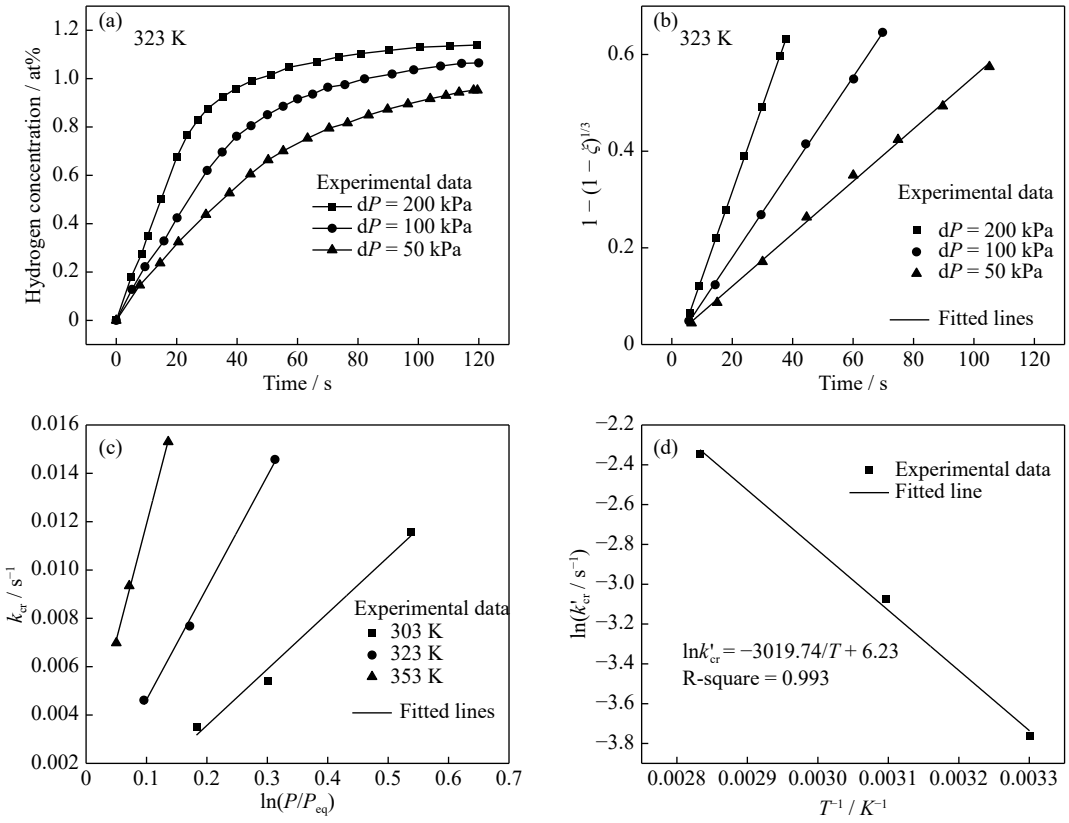


**Fig. 8. (a) Kinetic curves of $LaNi_5$ at different pressure differences d$P$ of hydrogen absorption pressure and equilibrium pressure; (b) curves of $1-(1-\xi)^{1/3}$ and $t$ at different pressure differences; (c) curves of $k_{cr}$ with $\ln(P/P_{eq})$ at different temperatures; (d) curves of $k'_{cr}$ with $1/T$. (a) Reprinted from *J. Less Common Met.*, 89, M. Miyamoto, K. Yamaji, and Y. Nakata, Reaction kinetics of $LaNi_5$, 111-116, Copyright 1983, with permission from Elsevier.**

ferent temperatures, the values of $k_{cr}$ and $k'_{cr}$ can be determined. Then, the curve of $\ln k'_{cr}$ and $1/T$ can be plotted in Fig. 8(d). According to the fitted result, the values of $E$ and $k_{cr,0}$ can be calculated as 32.2 kJ·mol$^{-1}$ and 507.75 s$^{-1}$, respectively. Thus, the kinetic equation of $LaNi_5$ can be written as follows:

$$1-(1-\xi)^{1/3}=507.75\exp\left(-\frac{3019.74}{T}\right)\ln(P/P_{eq})t \quad (49)$$

However, different researchers have different estimations of the RCS of the hydrogen absorption process of $LaNi_5$ alloy [24,75−80]. Table 3 shows some published results for the RCS of $LaNi_5$ alloys. Although the composition of $LaNi_5$ alloy is the same, the RCS and activation energy evaluated by different researchers are different. This finding indicates that the hydriding/dehydriding kinetic mechanism of HSA is complex, which is related not only to the composition but also to the test conditions, preparation method of the alloy, particle and its surface states, and impurity. Thus, researchers should consider these factors when analyzing the kinetic mechanism and refer to other published works. Other characterization methods, such as SEM and TEM, are necessary [74,81].

**Table 3. Hydrogen absorption kinetic mechanism and activation energy of $LaNi_5$ alloys**

| No. | Test conditions | Kinetic model | RCS | $E$ / (kJ·mol$^{-1}$) | Ref. |
|---|---|---|---|---|---|
| 1 | 288–353 K, <1 MPa | CV | Chemical reaction | 32.2 | [75] |
| 2 | 273–363 K, 0.5 MPa | — | Nucleation and growth | 31.8 | [76] |
| 3 | 333–338 K, 2 MPa | — | Mixed (chemisorption and diffusion of hydrogen) | — | [77] |
| 4 | 298–323 K, $P_r$ = 2–5[a] | C-JMAK ($n$ = 1) | Nucleation and growth (one-dimensional diffusion) | 27 | [78] |
| 5 | 298–313 K, $P_r$ = 2–5 | C-JMAK ($n$ = 1) | Nucleation and growth (one-dimensional diffusion) | 30–40 | [79] |
| 6 | 303–333 K, $P_r$ = 2 | Jander | Diffusion of hydrogen | 27.7 | [80] |
| 7 | 303 K, 0.6–1 MPa | Chou | Diffusion of hydrogen | — | [24] |

Note: [a] $P_r$ is the ratio of pressure to equilibrium pressure.

The substitution of alloying elements can change the RCS and activation energy of the hydrogen absorption and desorption processes in $AB_5$ alloys [49,82−84]. The $LaNi_{5-x}Al_x$ alloy is a common ternary $AB_5$ alloy [82]. Fig. 9 shows the hydrogen absorption and desorption pressure curves of $LaNi_{4.25}Al_{0.75}$ [49] at different temperatures and particle radii tested by the flowing volumetric method. The fitted results indicate that the RCSs for the hydrogen absorption process of $LaNi_{4.25}Al_{0.75}$ at different pressure ranges are surface permeation and nucleation and growth of MH, whereas the RCS for the hydrogen desorption process is only the nucleation and growth of MH.

Moreover, because of the high cost of the elementary substance La, the mixed rare earth Mm can be used to replace La [85−86]. The RCS of $MmNi_5$ alloy can be determined based on the curves of $\partial\xi/\partial t$ and $\xi$. Notably, the RCS of the hydrogen absorption process changes with the pressure and reaction fraction [50], as shown in Fig. 10. The lines are re-plotted according to the kinetic equations (6)−(8) given in Ref. [50]. At the initial stage of the hydrogen absorption reaction ($\xi$ < 0.35), when the hydrogen absorption pressure $P$ is low and close to the equilibrium pressure of 1 MPa ($P \le 1.5$ MPa), the RCS is surface permeation. When the hydrogen absorption pressure continues to increase, the RCS will change to nucleation and growth ($n \approx 1.55$). With the further increase of the reaction fraction ($\xi$ > 0.4), the RCS changes from surface penetration (or nucleation and growth) to the diffusion of hydrogen.

### 4.2. $AB_2$-type HSAs

The $AB_2$-type alloy has a Laves phase structure [87], such as Zr-based [23,88−89] and Ti-based alloy [90−91]. $Ti_{1.02}Cr_{1.0}Fe_{0.7-x}Mn_{0.3}Al_x$ ($0 \le x \le 0.1$) is a typical Zr-based alloy, and its hydrogen desorption process can be described by the C-JMAK model ($n$ = 1). The RCS is the nucleation and growth of MH (one-dimensional diffusion), and the activation energy is within 7.4−9.9 kJ·mol$^{-1}$ [92]. Moreover, because of the complex phase composition of $AB_2$-type alloy with multiple MH phases, the hydrogen absorption and desorption mechanism may change with the processes of the hydrogen absorption and desorption reactions. The hydrogen absorption process of $Zr_{0.2}Ho_{0.8}Fe_2$ alloy has two hydrogen absorption stages [93]. Although both stages can be fitted by the C-JMAK model ($n$ = 1), the rate constant and activation energy are different. The activation energies of both stages are 24 and 2 kJ·mol$^{-1}$ [93].

### 4.3. AB-type HSAs

ZrCo-based alloy is one of the typical AB-type HSA, and the RCS of the hydrogen absorption reaction in the temperature range of 544−603 K is nucleation and growth with the activation energy of 120 kJ·mol$^{-1}$ [61]. The fluorinated and Ni-plated ZrCo alloys are controlled by chemisorption, but the hydrogen absorption kinetics of Ni-plated ZrCo alloys is significantly improved because of the easy dissociation of $H_2$ on Ni at the particle surface [94]. The C-JMAK model is used to analyze the hydrogen absorption kinetics curves of the $ZrCo_{0.95}Cr_{0.05}$ alloy [95]. The fitted results show that the values of $n$ for $ZrCo_{0.95}Cr_{0.05}$ at 373, 348, and 323 K are 2.83, 1.36, and 1.07, respectively. Notably, with the decrease of temperature, the RCS of the hydrogen absorption reaction of $ZrCo_{0.95}Cr_{0.05}$ changes from the three-dimensional diffusion to the one-dimensional diffusion of nucleation and growth.

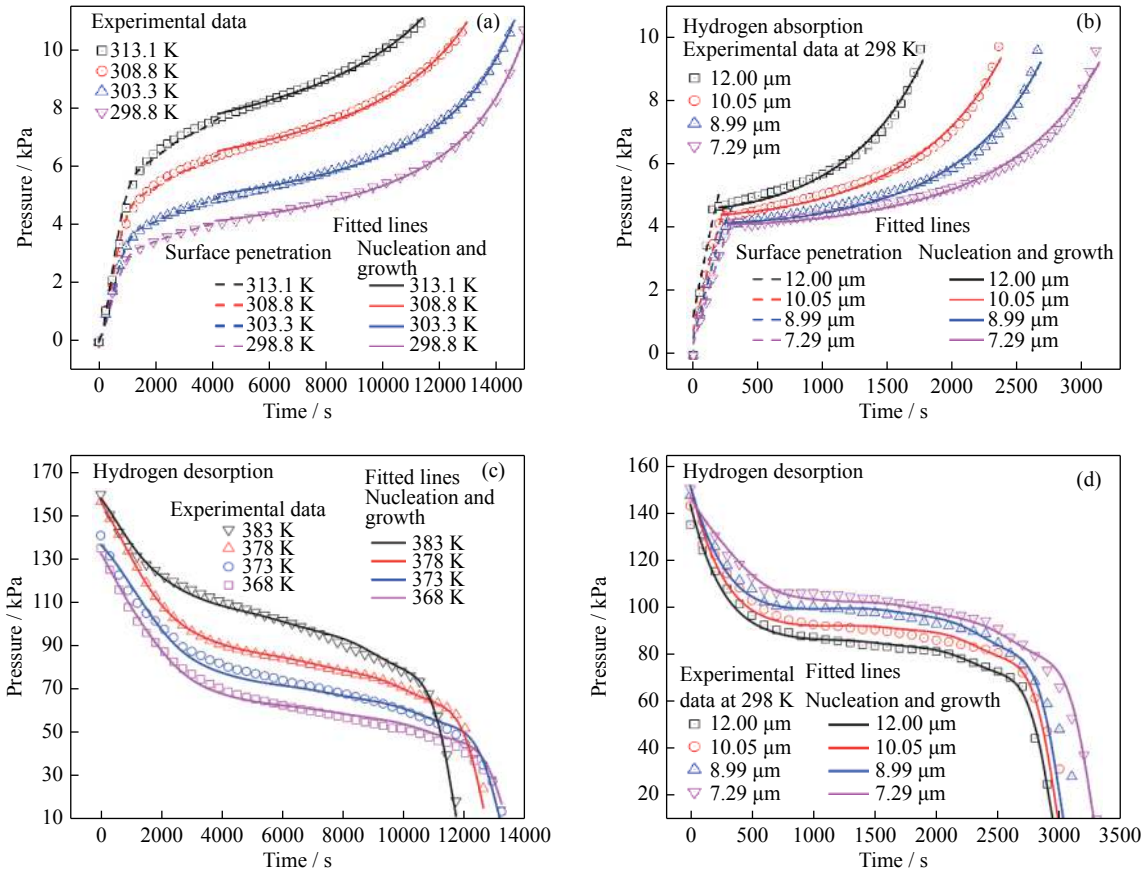


**Fig. 9. Pressure curves of $LaNi_{4.25}Al_{0.75}$: effects of temperature (a) and particle radius (b) on the hydrogen absorption process; effects of temperature (c) and particle radius (d) on the hydrogen desorption process. Reprinted from *Chem. Eng. J.*, 421, X. Lin, W. Xie, Q. Zhu, H.G. Yang, and Q. Li, Rational optimization of metal hydride tank with $LaNi_{4.25}Al_{0.75}$ as hydrogen storage medium, 127844, Copyright 2021, with permission from Elsevier.**

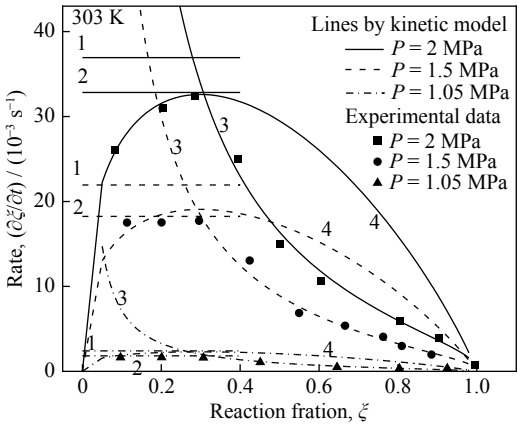


**Fig. 10. Curves of the hydrogen absorption rate and reaction fraction of the $MmNi_5$ alloy under different pressures (1—Chemisorption; 2—Surface penetration; 3—Diffusion of hydrogen; 4—Nucleation and growth). Adapted from [50].**

### 4.4. Mg-based HSAs

The kinetic properties of hydrogen absorption and desorption of pure Mg are poor but can be enhanced by alloying or adding catalysts [96–100]. Table 4 shows the kinetic results of Mg-based HSAs. For pure Mg, the hydrogen absorption reaction is initially controlled by chemisorption and subsequently controlled by the diffusion of hydrogen [109]. For $MgH_2$, the hydrogen absorption reaction is controlled by the diffusion of hydrogen [110]. Recently, Shriniwasan *et al.* [81,111] investigated the hydrogen absorption mechanism of Mg by combining SEM and kinetic analysis. They determined that the RCSs of Mg are chemisorption at the initial stage, followed by the movement of the interface during the nucleation and growth processes, and finally, the diffusion of hydrogen [81].

The alloying method can introduce a new phase to Mg [101,112–113], which can change/increase the reaction path of the hydrogen absorption and desorption processes [114–117], significantly reduce the activation energy and hydrogen desorption temperature of Mg alloy, and change the RCS. $Mg_2Ni$ is a typical binary Mg-based alloy [118–120]. The addition of Ni can considerably increase the rate of the hydrogen absorption and desorption reactions, and the temperature of the hydrogen desorption reaction of $Mg_2Ni$ is significantly lower than that of pure Mg. The rate of the hydrogen absorption reaction of $Mg_2Ni$ is linearly related to pressure, and the RCS is chemisorption with the activation energy of 19.6 $kJ \cdot mol^{-1}$ [121].

Generally, two or more elements, such as Nd, Ni, Ce, Y, La, In, and Ag, are added to Mg to improve the kinetic properties of the Mg alloy [55,66,98,117,122–123]. The $Mg_{18}In_1Ni_3$ alloy prepared by ball milling can absorb 3.8wt% hydrogen in 20 min at 553 K and desorb 1wt% hydrogen in 10 min at 493 K. The C-JMAK model was used to fit the hydrogen de-

**Table 4. Kinetic results of some Mg-based HSAs**

| No. | HSAs | Preparation methods | Test conditions | Kinetic model | RCS | $E$ / (kJ·mol$^{-1}$) | Ref. |
|---|---|---|---|---|---|---|---|
| 1 | Mg−30wt% $LaNi_5$ | MA; HC | 302−423 K, 1 MPa | Chou | Surface penetration; Diffusion of hydrogen | 28.0 (ab); 25.2 (ab) | [25] |
| 2 | $La_{1.5}Ni_{0.5}Mg_{17}$ | HC | 523−573 K, 0.755 MPa | Jander | Diffusion of hydrogen | 90 (ab) | [60] |
| 3 | $Nd_4Mg_{80}Ni_8$ | Melting | 373−623 K, 3.4 MPa; 564−620 K, Vacuum | Chou | Diffusion of hydrogen (ab); Surface penetration (de) | 82.3 (ab) 97.5 (de) | [101] |
| 4 | $Mg_{18}In_1Ni_3$ | MA | 493−583 K, Vacuum | C-JMAK ($n$ = 1) | Nucleation and growth (one-dimensional diffusion) | 107 (de) | [102] |
| 5 | $LaNiMg_{17}$ | MA | 553−623 K, 0.755 MPa | Chou | Diffusion of hydrogen | 71 (ab) | [103] |
| 6 | Mg−$Y_2O_3$; Mg−Y | Arc melting | 473−573 K, 3 MPa | C-JMAK | — | 79.9 (ab) 56.2 (ab) | [104] |
| 7 | $Mg_{80}Ce_{18}Ni_2$ | Melting | 523−585 K, 3.5 MPa | C-JMAK ($n$ = 0.53) | Nucleation and growth (one-dimensional diffusion) | 63 (de) | [105] |
| 8 | $Mg_{12}NiY$ | Melting | 523−623 K, Vacuum | C-JMAK ($n$ = 0.6−0.8) | — | 44.96 (de) | [106] |
| 9 | $Mg_2In_{0.1}Ni$ | Melting | 467−507 K, Vacuum | C-JMAK ($n$ = 0.6−0.8) | Nucleation and growth (one-dimensional diffusion) | 28.9 (de) | [107] |
| 10 | Mg−$TiH_{1.971}$−$TiH_{1.5}$ | HC | 298−673 K, 4 MPa; 473−673 K, Vacuum | C-JMAK ($n$ = 0.3−1.1) | Nucleation and growth (one-dimensional diffusion) | 12.5 (ab); 46.2 (de) | [108] |

sorption kinetic curves, and the values of $n$ are close to 1, indicating that the RCS was the one-dimensional diffusion of nucleation and growth [102]. The calculated activation energy was 107 kJ·mol$^{-1}$, which was lower than the 160 kJ·mol$^{-1}$ of pure Mg [41]. The Chou, Jander, and C-JMAK models have been used to systematically analyze the hydrogen absorption and desorption kinetics of Mg−Ni−La [60,103], Mg−Ni−Ce [124], and Mg−Ni−Nd [101]. The kinetic properties of the $LaNiMg_{17}$ alloy prepared by the mechanical alloying (MA) method are improved because of the introduction of surface defects. The RCS of the hydrogen absorption and desorption reaction is the diffusion of hydrogen. The activation energy of the hydrogen absorption reaction of the $LaNiMg_{17}$ alloy prepared by the MA method is 71 kJ·mol$^{-1}$ [103], whereas that of the $La_{1.5}Ni_{0.5}Mg_{17}$ alloy prepared by the hydriding combustion (HC) method is 90 kJ·mol$^{-1}$ [60]. The hydrogen absorption reaction of the $Nd_4Mg_{80}Ni_8$ alloy is controlled by the diffusion of hydrogen with the activation energy of 82.3 kJ·mol$^{-1}$ , whereas the hydrogen desorption reaction of the $Nd_4Mg_{80}Ni_8$ alloy is controlled by surface penetration with the activation energy of 97.5 kJ·mol$^{-1}$ [101].

The addition of a catalyst to Mg is a common method to improve the kinetic performance of the hydrogen absorption and desorption reactions [125]. The catalysts mainly include oxides, complex hydrides, and La and Ni compounds [104,126−128]. For Mg−$Y_2O_3$ and Mg−Y composite powders prepared by arc plasma melting, Mg−$Y_2O_3$ can adsorb 5wt% (573 K) hydrogen at 100 s, whereas Mg−Y only adsorbs 2.3wt% hydrogen under the same conditions [104]. The C-JMAK model was used to analyze the kinetics of the two powders, and the values of activation energy were 79.9 and 56.2 kJ·mol$^{-1}$. The high pre-exponential factor was the reason for the fast hydrogen absorption rate of Mg−$Y_2O_3$ [104]. The hydrogen absorption kinetics of Mg−$x$wt%$LaNi_5$ ($x$ = 10−50) composites prepared by the MA, microwave sintering, and traditional sintering methods were determined as follows [25]: (1) The RCS of Mg−$x$wt%$LaNi_5$ was the diffusion of hydrogen, and the kinetic properties of Mg−$x$wt% $LaNi_5$ were enhanced with the increase of $LaNi_5$ content. (2) Mg−30wt%$LaNi_5$ prepared by mechanical ball milling was controlled by surface penetration, whereas the alloys prepared by HC and microwave sintering were controlled by the diffusion of hydrogen atoms. The hydrogen absorption and desorption rates and the kinetic mechanism can be influenced by the amount of catalyst or catalytic phase and the preparation method.

## 5. Summary and prospects

Kinetics is significant for the development of HSA and the design of the HST using numerical simulation. In this paper, we review the kinetic models and their corresponding analysis procedures, as well as their applications to HSA. The development of theoretical kinetic models lagged behind experimental investigations. Many kinetic models only use the rate constant to express the effect of temperature or pressure on reaction rate, and only a few models can express the relationship between reaction fraction and multiple factors, such as temperature, pressure, and particle size. Most kinetic models are constructed based on the isothermal process, and only the NI-JMAK model can extend to the non-isothermal condition using the parameters obtained from the isothermal condition. The application of kinetic models faces the problem that some kinetic models are presented as differential equations of reaction rate, which cannot be conveniently applied in practice. Therefore, a model that has analytical formulas, is applicable under isothermal and non-isothermal conditions, and considers multiple factors is desirable for further hydrogenation and dehydrogenation kinetic analysis.

The kinetic mechanism of the hydrogen absorption and desorption reactions of $AB_5$-type, $AB_2$-type, AB-type, and Mg-based HSAs is not the same, which is related to the composition of the alloys, preparation methods, powder particle states, type and content of catalysts, and test conditions of hydrogen absorption and desorption. In general, alloying and adding catalysts can improve the hydrogen absorption and desorption kinetics of the alloy and reduce the activation energy but do not necessarily change the RCS. According to the current research results, most of the hydrogen absorption and desorption processes are controlled by the diffusion of hydrogen or the nucleation and growth of MH. Thus, we propose the use of the kinetic models for the diffusion of hydrogen or the nucleation and growth processes to analyze the experimental data and the use of other kinetic models for other RCSs. After obtaining the best-fit model, the kinetic parameters, such as the rate constant, activation energy, Avrami exponent, and forms of the pressure and particle radius terms, can be determined according to the fitted results. Notably, accurate and unambiguous experimental data are the prerequisite for kinetic analysis. Then, the accurate kinetic equation and its parameters can be used in the mathematical model to design the HST. In the future, a high-accuracy and concise kinetic model is necessary to describe the actual hydrogen absorption and desorption processes of HSA. The kinetic analysis may be combined with *in situ* experiments or molecular dynamics theory to explain the kinetic mechanism. We believe that this review is helpful for researchers focusing on the kinetic mechanism of HSA or the design of the HST by providing systematic fundamentals, analysis procedures, and application of kinetic models.

## Acknowledgements

This work was financially supported by the Chongqing Special Key Project of Technology Innovation and Application Development, China (No. cstc2019jscx-dxwtB0029), the National Natural Science Foundation of China (Nos. 51871143 and U2102212), the Science and Technology Committee of Shanghai, China (No. 19010500400), and the Shanghai Rising-Star Program (No. 21QA1403200).

## Conflict of Interest

All authors certify that they have no affiliations with or involvement in any organization or entity with any financial interest or non-financial interest in the subject matter or materials discussed in this manuscript.

## References

[1] B. Sakintuna, F. Lamari-Darkrim, and M. Hirscher, Metal hydride materials for solid hydrogen storage: A review, *Int. J. Hydrogen Energy*, 32(2007), No. 9, p. 1121.

[2] T.Y. Wei, K.L. Lim, Y.S. Tseng, and S.L.I. Chan, A review on the characterization of hydrogen in hydrogen storage materials, *Renewable Sustainable Energy Rev.*, 79(2017), p. 1122.

[3] Y. Li, L.N. Cheng, W.K. Miao, C.X. Wang, D.Z. Kuang, and S.M. Han, Nd−Mg−Ni alloy electrodes modified by reduced graphene oxide with improved electrochemical kinetics, *Int. J. Miner. Metall. Mater.*, 27(2020), No. 3, p. 391.

[4] H.Q. Nguyen and B. Shabani, Proton exchange membrane fuel cells heat recovery opportunities for combined heating/cooling and power applications, *Energy Convers. Manage.*, 204(2020), art. No. 112328.

[5] C.S. Park, K. Jung, S.U. Jeong, K.S. Kang, Y.H. Lee, Y.S. Park, and B.H. Park, Development of hydrogen storage reactor using composite of metal hydride materials with ENG, *Int. J. Hydrogen Energy*, 45(2020), No. 51, p. 27434.

[6] X. Lin, H.G. Yang, Q. Zhu, and Q. Li, Numerical simulation of a metal hydride tank with $LaNi_{4.25}Al_{0.75}$ using a novel kinetic model at constant flows, *Chem. Eng. J.*, 401(2020), art. No. 126115.

[7] Y. Ye, J.F. Lu, J. Ding, W.L. Wang, and J.Y. Yan, Numerical simulation on the storage performance of a phase change materials based metal hydride hydrogen storage tank, *Appl. Energy*, 278(2020), art. No. 115682.

[8] W.C. He, X.W. Lü, C.Y. Ding, and Z.M. Yan, Oxidation pathway and kinetics of titania slag powders during cooling process in air, *Int. J. Miner. Metall. Mater.*, 28(2021), No. 6, p. 981.

[9] X.Y. Shen, Y.Y. Liang, H.M. Shao, Y. Sun, Y. Liu, and Y.C. Zhai, Extraction and kinetic analysis of Pb and Sr from the leaching residue of zinc oxide ore, *Int. J. Miner. Metall. Mater.*, 28(2021), No. 2, p. 201.

[10] M.M. Sun, J.L. Zhang, K.J. Li, K. Guo, Z.M. Wang, and C.H. Jiang, Gasification kinetics of bulk coke in the $CO_2$/CO/$H_2$/$H_2O$/$N_2$ system simulating the atmosphere in the industrial blast furnace, *Int. J. Miner. Metall. Mater.*, 26(2019), No. 10, p. 1247.

[11] X.F. Zhu, T.A. Zhang, and G.Z. Lü, Kinetics of carbonated decomposition of hydrogarnet with different silica saturation coefficients, *Int. J. Miner. Metall. Mater.*, 27(2020), No. 4, p. 472.

[12] C.S. Wang, X.H. Wang, Y.Q. Lei, C.P. Chen, and Q.D. Wang, The hydriding kinetics of $MlNi_5$—I. Development of the model, *Int. J. Hydrogen Energy*, 21(1996), No. 6, p. 471.

[13] T.Z. Si, X.Y. Zhang, J.J. Feng, X.L. Ding, and Y.T. Li, Enhancing hydrogen sorption in $MgH_2$ by controlling particle size and contact of Ni catalysts, *Rare Met.*, 40(2021), No. 4, p. 995.

[14] Y.P. Pang and Q. Li, A review on kinetic models and corresponding analysis methods for hydrogen storage materials, *Int. J. Hydrogen Energy*, 41(2016), No. 40, p. 18072.

[15] G. Chen, Y. Zhang, J. Chen, X.L. Guo, Y.F. Zhu, and L.Q. Li, Enhancing hydrogen storage performances of $MgH_2$ by Ni nano-particles over mesoporous carbon CMK-3, *Nanotechnol.*, 29(2018), No. 26, art. No. 265705.

[16] L.E.R. Vega, D.R. Leiva, R.M. Leal Neto, W.B. Silva, R.A. Silva, T.T. Ishikawa, C.S. Kiminami, and W.J. Botta, Improved ball milling method for the synthesis of nanocrystalline TiFe compound ready to absorb hydrogen, *Int. J. Hydrogen Energy*, 45(2020), No. 3, p. 2084.

[17] H.Q. Kou, H. He, W.H. Luo, T. Tang, Z.Y. Huang, H. Wang, J.C. Bao, Y. Xue, S.H. Pei, and W.D. Liu, Effects of ball milling on hydrogen sorption properties and microstructure of ZrCo alloy, *Fusion Eng. Des.*, 138(2019), p. 68.

[18] W. Jander, Reaktionen im festen Zustande Bei höheren Temperaturen. Reaktionsgeschwindigkeiten endotherm verlaufender Umsetzungen, *Z. Anorg. Allg. Chem.*, 163(1927), No. 1, p. 1.

[19] Z.J. Cao, L.Z. Ouyang, H. Wang, J.W. Liu, L.X. Sun, M. Felderhoff, and M. Zhu, Development of ZrFeV alloys for hybrid hydrogen storage system, *Int. J. Hydrogen Energy*, 41(2016),

No. 26, p. 11242.
[20] K.C. Chou, Q. Li, Q. Lin, L.J. Jiang, and K.D. Xu, Kinetics of absorption and desorption of hydrogen in alloy powder, *Int. J. Hydrogen Energy*, 30(2005), No. 3, p. 301.
[21] Q. Li, K.C. Chou, Q. Lin, L.J. Jiang, and F. Zhan, Influence of the initial hydrogen pressure on the hydriding kinetics of the $Mg_{2-x}Al_xNi$ ($x$ = 0, 0.1) alloys, *Int. J. Hydrogen Energy*, 29(2004), No. 13, p. 1383.
[22] Q. Luo, X.H. An, Y.B. Pan, X. Zhang, J.Y. Zhang, and Q. Li, The hydriding kinetics of Mg-Ni based hydrogen storage alloys: A comparative study on Chou model and Jander model, *Int. J. Hydrogen Energy*, 35(2010), No. 15, p. 7842.
[23] X.Y. Cui, Q. Li, K.C. Chou, S.L. Chen, G.W. Lin, and K.D. Xu, A comparative study on the hydriding kinetics of Zr-based $AB_2$ hydrogen storage alloys, *Intermetallics*, 16(2008), No. 5, p. 662.
[24] X.H. An, Y.B. Pan, Q. Luo, X. Zhang, J.Y. Zhang, and Q. Li, Application of a new kinetic model for the hydriding kinetics of $LaNi_{5-x}Alx$ ($0 \leq x \leq 1.0$) alloys, *J. Alloys Compd.*, 506(2010), No. 1, p. 63.
[25] Y.B. Pan, Y.F. Wu, and Q. Li, Modeling and analyzing the hydriding kinetics of Mg–$LaNi_5$ composites by Chou model, *Int. J. Hydrogen Energy*, 36(2011), No. 20, p. 12892.
[26] Q. Li, L.J. Jiang, K.C. Chou, Q. Lin, F. Zhan, K.D. Xu, X.G. Lu, and J.Y. Zhang, Effect of hydrogen pressure on hydriding kinetics in the $Mg_{2-x}Ag_xNi$-H (x = 0.05, 0.1) system, *J. Alloys Compd.*, 399(2005), No. 1-2, p. 101.
[27] Q. Luo, J.D. Li, B. Li, B. Liu, H.Y. Shao, and Q. Li, Kinetics in Mg-based hydrogen storage materials: Enhancement and mechanism, *J. Magnesium Alloys*, 7(2019), No. 1, p. 58.
[28] Y.P. Pang, D.K. Sun, Q.F. Gu, K.C. Chou, X.L. Wang, and Q. Li, Comprehensive determination of kinetic parameters in solid-state phase transitions: An extended jonhson–mehl–avrami–kolomogorov model with analytical solutions, *Cryst. Growth Des.*, 16(2016), No. 4, p. 2404.
[29] Q. Luo, Q.F. Gu, B. Liu, T.F. Zhang, W.Q. Liu, and Q. Li, Achieving superior cycling stability by *in situ* forming $NdH_2$–Mg–$Mg_2Ni$ nanocomposites, *J. Mater. Chem. A*, 6(2018), No. 46, p. 23308.
[30] Y.H. Zhang, W. Zhang, J.L. Gao, X. Wei, T.T. Zhai, and Y. Cai, Improved hydrogen storage kinetics of Mg-based alloys by substituting La with Sm, *Int. J. Hydrogen Energy*, 45(2020), No. 41, p. 21588.
[31] X.L. Yang, Q.H. Hou, L.B. Yu, and J.Q. Zhang, Improvement of the hydrogen storage characteristics of $MgH_2$ with a flake Ni nano-catalyst composite, *Dalton Trans.*, 50(2021), No. 5, p. 1797.
[32] Y.H. Zhang, X. Wei, W. Zhang, Z.M. Yuan, J.L. Gao, Y. Qi, and H.P. Ren, Effect of milling duration on hydrogen storage thermodynamics and kinetics of Mg-based alloy, *Int. J. Hydrogen Energy*, 45(2020), No. 58, p. 33832.
[33] K.C. Chou and K.D. Xu, A new model for hydriding and dehydriding reactions in intermetallics, *Intermetallics*, 15(2007), No. 5-6, p. 767.
[34] A. Khawam and D.R. Flanagan, Solid-state kinetic models: Basics and mathematical fundamentals, *J. Phys. Chem. B*, 110(2006), No. 35, p. 17315.
[35] J. Bloch and M.H. Mintz, Kinetics and mechanisms of metal hydrides formation—A review, *J. Alloys Compd.*, 253-254(1997), p. 529.
[36] J.F. Song, J. She, D.L. Chen, and F.S. Pan, Latest research advances on magnesium and magnesium alloys worldwide, *J. Magnesium Alloys*, 8(2020), No. 1, p. 1.
[37] W. Jiang, H. Wang, and M. Zhu, $AlH_3$ as a hydrogen storage material: Recent advances, prospects and challenges, *Rare Met.*, 40(2021), No. 12, p. 3337.
[38] P.S. Rudman, Hydriding and dehydriding kinetics, *J. Less Common Met.*, 89(1983), No. 1, p. 93.
[39] D.P. Broom, *Hydrogen Storage Materials: The Characterisation of Their Storage Properties*, Springer, London, 2011.
[40] C. Aharoni and F.C. Tompkins, Kinetics of adsorption and desorption and the elovich equation, *Adv. Catal.*, 21(1970), p. 1.
[41] A. Ginstling and B. Brounshtein, Concerning the diffusion kinetics of reactions in spherical particles, *J. Appl. Chem. USSR*, 23(1950), p. 1327.
[42] R.E. Carter, Kinetic model for solid-state reactions, *J. Chem. Phys.*, 34(1961), No. 6, p. 2010.
[43] F. Booth, A note on the theory of surface diffusion reactions, *Trans. Faraday Soc.*, 44(1948), art. No. 796.
[44] K.C. Chou, Q. Luo, Q. Li, and J.Y. Zhang, Influence of the density of oxide on oxidation kinetics, *Intermetallics*, 47(2014), p. 17.
[45] J. Crank, *The Mathematics of Diffusion*, 2nd ed., Oxford university press, London, 1979.
[46] A.T.W. Kempen, F. Sommer, and E.J. Mittemeijer, Determination and interpretation of isothermal and non-isothermal transformation kinetics; the effective activation energies in terms of nucleation and growth, *J. Mater. Sci.*, 37(2002), No. 7, p. 1321.
[47] J.W. Christian, Eutectoidal transformations, [in] *The Theory of Transformations in Metals and Alloys*, Amsterdam, Elsevier, 2002, p. 797.
[48] J.T. Carstensen, Stability of solids and solid dosage forms, *J. Pharm. Sci.*, 63(1974), No. 1, p. 1.
[49] X. Lin, W. Xie, Q. Zhu, H.G. Yang, and Q. Li, Rational optimization of metal hydride tank with $LaNi_{4.25}Al_{0.75}$ as hydrogen storage medium, *Chem. Eng. J.*, 421(2021), art. No. 127844.
[50] X.H. Wang, C.S. Wang, C.P. Chen, Y.Q. Lei and Q.D. Wang, The hydriding kinetics of $MlNi_5$—II. Experimental results, *Int. J. Hydrogen Energy*, 21(1996), No. 6, p. 479.
[51] X. Lin, D.K. Sun, S.L. Chen, Q. Zhu, H.Y. Leng, and Q. Li, Numerical analysis on pulverization and self-densification for hydrogen storage performance of a metal hydride tank, *Appl. Therm. Eng.*, 161(2019), art. No. 114129.
[52] X. Lin, Q. Zhu, H.Y. Leng, H.G. Yang, T. Lyu, and Q. Li, Numerical analysis of the effects of particle radius and porosity on hydrogen absorption performances in metal hydride tank, *Appl. Energy*, 250(2019), p. 1065.
[53] J. Nam, J. Ko, and H. Ju, Three-dimensional modeling and simulation of hydrogen absorption in metal hydride hydrogen storage vessels, *Appl. Energy*, 89(2012), No. 1, p. 164.
[54] D. Wang, Y.Q. Wang, Z.N. Huang, F.S. Yang, Z. Wu, L. Zheng, L. Wu, and Z.X. Zhang, Design optimization and sensitivity analysis of the radiation mini-channel metal hydride reactor, *Energy*, 173(2019), p. 443.
[55] T. Yang, P. Wang, C.Q. Xia, Q. Li, C.Y. Liang, and Y.H. Zhang, Characterization of microstructure, hydrogen storage kinetics and thermodynamics of a melt-spun $Mg_{86}Y_{10}Ni_4$ alloy, *Int. J. Hydrogen Energy*, 44(2019), No. 13, p. 6728.
[56] Y.H. Zhang, X.F. Li, Y. Cai, Y. Qi, S.H. Guo, and D.L. Zhao, Improved hydrogen storage performances of Mg−Y−Ni−Cu alloys by melt spinning, *Renew. Energy*, 138(2019), p. 263.
[57] K.S. Nahm, W.Y. Kim, S.P. Hong, and W.Y. Lee, The reaction kinetics of hydrogen storage in $LaNi_5$, *Int. J. Hydrogen Energy*, 17(1992), No. 5, p. 333.
[58] J.W. Oh, C.Y. Kim, K.S. Nahm, and K.S. Sim, The hydriding kinetics of $LaNi_{4.5}Al_{0.5}$ with hydrogen, *J. Alloys Compd.*, 278(1998), No. 1-2, p. 270.
[59] M.N. Mungole and R. Balasubramaniam, Hydrogen desorption kinetics in $MmNi_{4.2}Al_{0.8}$−H system, *Int. J. Hydrogen Energy*, 23(1998), No. 5, p. 349.
[60] Q. Li, Q. Lin, K.C. Chou, L.J. Jiang, and F. Zhan, Hydriding kinetics of the $La_{1.5}Ni_{0.5}Mg_{17}$−H system prepared by hydrid-

ing combustion synthesis, *Intermetallics*, 12(2004), No. 12, p. 1293.

[61] R.A. Jat, S.C. Parida, J. Nuwad, R. Agarwal, and S.G. Kulkarni, Hydrogen sorption−desorption studies on ZrCo−hydrogen system, *J. Therm. Anal. Calorim.*, 112(2013), No. 1, p. 37.

[62] L. Jai-Young, C.N. Park, and S.M. Pyun, The activation processes and hydriding kinetics of FeTi, *J. Less Common Met.*, 89(1983), No. 1, p. 163.

[63] E. Bershadsky, A. Klyuch, and M. Ron, Hydrogen absorption and desorption kinetics of $TiFe_{0.8}Ni_{0.2}H$, *Int. J. Hydrogen Energy*, 20(1995), No. 1, p. 29.

[64] R. Ramesh, Y.V.G.S. Murti, K.V. Reddy, K.V.S. Rama Rao, and T.P. Das, The kinetics of hydrogen absorption in $Zr_{1-x}Ho_xCo_2$ ($x$ = 0.4, 0.6 and 0.8) alloys, *J. Alloys Compd.*, 205(1994), No. 1-2, p. 211.

[65] X.C. Kong, J.L. Du, K. Wang, Z.L. Li, and Z. Wu, Kinetics of hydrogen absorption for $Ti_{33}V_{20}Cr_{47}$ alloy powder, *Rare Met. Mater. Eng.*, 41(2012), No. 11, p. 1899.

[66] Q. Li, K.C. Chou, Q. Lin, L.J. Jiang, and F. Zhan, Hydrogen absorption and desorption kinetics of Ag−Mg−Ni alloys, *Int. J. Hydrogen Energy*, 29(2004), No. 8, p. 843.

[67] G. Liang, J. Huot, S. Boily, A. Van Neste, and R. Schulz, Hydrogen storage properties of the mechanically milled $MgH_2$−V nanocomposite, *J. Alloys Compd.*, 291(1999), No. 1-2, p. 295.

[68] G. Liang, J. Huot, S. Boily, and R. Schulz, Hydrogen desorption kinetics of a mechanically milled $MgH_2$+5at.%V nanocomposite, *J. Alloys Compd.*, 305(2000), No. 1-2, p. 239.

[69] E. Akiba, K. Nomura, S. Ono, and S. Suda, Kinetics of the reaction between Mg–Ni alloys and $H_2$, *Int. J. Hydrogen Energy*, 7(1982), No. 10, p. 787.

[70] R.D. Penzhorn, M. Sirch, A.N. Perevezentsev, and A.N. Borisenko, Hydrogen sorption rate by intermetallic compounds suitable for tritium storage, *Fusion Technol.*, 28(1995), No. 3P2, p. 1399.

[71] E. Bershadsky, Y. Josephy, and M. Ron, Investigation of kinetics and structural changes in $TiFe_{0.8}$ $Ni_{0.2}$ after prolonged cycling, *J. Less Common Met.*, 172-174(1991), p. 1036.

[72] Y.F. Liu, K. Zhong, K. Luo, M.X. Gao, H.G. Pan, and Q.D. Wang, Size-dependent kinetic enhancement in hydrogen absorption and desorption of the Li–Mg–N–H system, *J. Am. Chem. Soc.*, 131(2009), No. 5, p. 1862.

[73] K. Zhong, Y.F. Liu, M.X. Gao, J.H. Wang, H. Miao, and H.G. Pan, Electrochemical kinetic performance of V−Ti−based hydrogen storage alloy electrode with different particle sizes, *Int. J. Hydrogen Energy*, 33(2008), No. 1, p. 149.

[74] S. Shriniwasan, H.Y. Tien, M. Tanniru, and S.S.V. Tatiparti, On the parameters of Johnson-Mehl-Avrami-Kolmogorov equation for the hydride growth mechanisms: A case of $MgH_2$, *J. Alloys Compd.*, 742(2018), p. 1002.

[75] M. Miyamoto, K. Yamaji, and Y. Nakata, Reaction kinetics of $LaNi_5$, *J. Less Common Met.*, 89(1983), No. 1, p. 111.

[76] O. Boser, Hydrogen sorption in $LaNi_5$, *J. Less Common Met.*, 46(1976), No. 1, p. 91.

[77] P.D. Goodell and P.S. Rudman, Hydriding and dehydriding rates of the $LaNi_5$−H system, *J. Less Common Met.*, 89(1983), No. 1, p. 117.

[78] J.T. Koh, A.J. Goudy, P. Huang, and G. Zhou, A comparison of the hydriding and dehydriding kinetics of $LaNI_5$ hydride, *J. Less Common Met.*, 153(1989), No. 1, p. 89.

[79] A. Zarynow, A.J. Goudy, R.G. Schweibenz, and K.R. Clay, The effect of the partial replacement of nickelin $LaNi_5$ hydride with iron, cobalt, and copper on absorption and desorption kinetics, *J. Less Common Met.*, 172-174(1991), p. 1009.

[80] P. Muthukumar, A. Satheesh, M. Linder, R. Mertz, and M. Groll, Studies on hydriding kinetics of some La-based metal hydride alloys, *Int. J. Hydrogen Energy*, 34(2009), No. 17, p. 7253.

[81] S. Shriniwasan, H. Goswami, H.Y. Tien, M. Tanniru, F. Ebrahimi, and S.S.V. Tatiparti, Contributions of multiple phenomena towards hydrogenation: A case of Mg, *J. Alloys Compd.*, 40(2015), No. 39, p. 13518.

[82] G.L. Liu, D.M. Chen, Y.M. Wang, and K. Yang, Experimental and computational investigations of $LaNi_{5-x}Al_x$ ($x$ = 0, 0.25, 0.5, 0.75 and 1.0) tritium-storage alloys, *J. Mater. Sci. Technol.*, 34(2018), No. 9, p. 1699.

[83] X.L. Wang and S. Suda, Effects of Al-substitution on hydriding reaction rates of $LaNi_{5-x}$Alx, *J. Alloys Compd.*, 191(1993), No. 1, p. 5.

[84] J.M. Joubert, V. Paul-Boncour, F. Cuevas, J.X. Zhang, and M. Latroche, $LaNi_5$ related $AB_5$ compounds: Structure, properties and applications, *J. Alloys Compd.*, 862(2021), art. No. 158163.

[85] R. Balasubramaniam, M.N. Mungole, and K.N. Rai, Hydriding properties of $MmNi_5$ system with aluminium, manganese and tin substitutions, *J. Alloys Compd.*, 196(1993), No. 1-2, p. 63.

[86] M. Jurczyk, W. Rajewski, W. Majchrzycki, and G. Wójcik, Mechanically alloyed $MmNi_5$-type materials for metal hydride electrodes, *J. Alloys Compd.*, 290(1999), No. 1-2, p. 262.

[87] M. Kandavel, V.V. Bhat, A. Rougier, L. Aymard, G.A. Nazri, and J.M. Tarascon, Improvement of hydrogen storage properties of the $AB_2$ Laves phase alloys for automotive application, *Int. J. Hydrogen Energy*, 33(2008), No. 14, p. 3754.

[88] F.C. Ruiz, E.B. Castro, H.A. Peretti, and A. Visintin, Study of the different $Zr_xNi_y$ phases of Zr-based $AB_2$ materials, *Int. J. Hydrogen Energy*, 35(2010), No. 18, p. 9879.

[89] C.B. Wan, X.P. Jiang, X.H. Yin, and X. Ju, High-capacity Zr-based $AB_2$-type alloys as metal hydride battery anodes, *J. Alloys Compd.*, 828(2020), art. No. 154402.

[90] Y.H. Xu, C.P. Chen, X.L. Wang, Y.Q. Lei, and Q.D. Wang, The cycle life and surface properties of Ti-based $AB_2$ metal hydride electrodes, *J. Alloys Compd.*, 337(2002), No. 1-2, p. 214.

[91] U. Ulmer, M. Dieterich, A. Pohl, R. Dittmeyer, M. Linder, and M. Fichtner, Study of the structural, thermodynamic and cyclic effects of vanadium and titanium substitution in laves-phase $AB_2$ hydrogen storage alloys, *Int. J. Hydrogen Energy*, 42(2017), No. 31, p. 20103.

[92] J.G. Li, Y.R. Guo, X.J. Jiang, S. Li, and X.G. Li, Hydrogen storage performances, kinetics and microstructure of $Ti_{1.02}Cr_{1.0}Fe_{0.7-x}Mn_{0.3}Al_x$ alloy by Al substituting for Fe, *Renew. Energy*, 153(2020), p. 1140.

[93] T.R. Kesavan, S. Ramaprabhu, K.V.S. Rama Rao, and T.P. Das, Hydrogen absorption and kinetic studies in $Zr_{0.2}Ho_{0.8}Fe_2$, *J. Alloys Compd.*, 244(1996), No. 1-2, p. 164.

[94] F. Wang, R.F. Li, C.P. Ding, J. Wan, R.H. Yu, and Z.M. Wang, Effect of catalytic Ni coating with different depositing time on the hydrogen storage properties of ZrCo alloy, *Int. J. Hydrogen Energy*, 41(2016), No. 39, p. 17421.

[95] L.L. Luo, X.Q. Ye, G.H. Zhang, H.Q. Kou, R.J. Xiong, G. Sang, R.H. Yu, and D.L. Zhao, Enhancement of hydrogenation kinetics and thermodynamic properties of $ZrCo_{1-x}$ Cr x ($x$ = 0–0.1) alloys for hydrogen storage, *Chin. Phys. B*, 29(2020), No. 8, art. No. 088801.

[96] J. Zhang, S. Yan, G.L. Xia, X.J. Zhou, X.Z. Lu, L.P. Yu, X.B. Yu, and P. Peng, Stabilization of low-valence transition metal towards advanced catalytic effects on the hydrogen storage performance of magnesium hydride, *J. Magnesium Alloys*, 9(2021), No. 2, p. 647.

[97] P.Y. Yao, Y. Jiang, Y. Liu, C.Z. Wu, K.C. Chou, T. Lyu, and Q. Li, Catalytic effect of Ni@rGO on the hydrogen storage properties of $MgH_2$, *J. Magnesium Alloys*, 8(2020), No. 2, p. 461.

[98] L.Z. Ouyang, F. Liu, H. Wang, J.W. Liu, X.S. Yang, L.X. Sun, and M. Zhu, Magnesium-based hydrogen storage compounds: A review, *J. Alloys Compd.*, 832(2020), art. No. 154865.
[99] M. Ismail, M.S. Yahya, N.A. Sazelee, N.A. Ali, F.A.H. Yap, and N.S. Mustafa, The effect of $K_2SiF_6$ on the $MgH_2$ hydrogen storage properties, *J. Magnesium Alloys*, 8(2020), No. 3, p. 832.
[100] P. Meena, R. Singh, V.K. Sharma, and I.P. Jain, Role of $NiMn_{9.3}Al_{4.0}Co_{14.1}Fe_{3.6}$ alloy on dehydrogenation kinetics of $MgH_2$, *J. Magnesium Alloys*, 6(2018), No. 3, p. 318.
[101] Q. Luo, Q.F. Gu, J.Y. Zhang, S.L. Chen, K.C. Chou, and Q. Li, Phase equilibria, crystal structure and hydriding/dehydriding mechanism of $Nd_4Mg_{80}Ni_8$ compound, *Sci. Rep.*, 5(2015), art. No. 15385.
[102] Y.S. Lu, M. Zhu, H. Wang, Z.M. Li, L.Z. Ouyang, and J.W. Liu, Reversible de-/hydriding characteristics of a novel $Mg_{18}In_1Ni_3$ alloy, *Int. J. Hydrogen Energy*, 39(2014), No. 26, p. 14033.
[103] Q. Li, K.C. Chou, K.D. Xu, Q. Lin, L.J. Jiang, and F. Zhan, Determination and interpretation of the hydriding and dehydriding kinetics in mechanically alloyed $LaNiMg_{17}$ composite, *J. Alloys Compd.*, 387(2005), No. 1-2, p. 86.
[104] S. Long, J.X. Zou, X. Chen, X.Q. Zeng, and W.J. Ding, A comparison study of Mg−$Y_2O_3$ and Mg−Y hydrogen storage composite powders prepared through arc plasma method, *J. Alloys Compd.*, 615(2014), p. S684.
[105] L.Z. Ouyang, X.S. Yang, M. Zhu, J.W. Liu, H.W. Dong, D.L. Sun, J. Zou, and X.D. Yao, Enhanced hydrogen storage kinetics and stability by synergistic effects of *in situ* formed $CeH_{2.73}$ and Ni in $CeH_{2.73}$−$MgH_2$−Ni nanocomposites, *J. Phys. Chem. C*, 118(2014), No. 15, p. 7808.
[106] Y. Sun, D.B. Wang, J.M. Wang, B.Z. Liu, and Q.M. Peng, Hydrogen storage properties of ultrahigh pressure $Mg_{12}NiY$ alloys with a superfine LPSO structure, *Int. J. Hydrogen Energy*, 44(2019), No. 41, p. 23179.
[107] L.Z. Ouyang, Z.J. Cao, H. Wang, J.W. Liu, D.L. Sun, Q.A. Zhang, and M. Zhu, Dual-tuning effect of In on the thermodynamic and kinetic properties of $Mg_2Ni$ dehydrogenation, *Int. J. Hydrogen Energy*, 38(2013), No. 21, p. 8881.
[108] T. Liu, C.G. Chen, F. Wang, and X.G. Li, Enhanced hydrogen storage properties of magnesium by the synergic catalytic effect of $TiH_{1.971}$ and $TiH_{1.5}$ nanoparticles at room temperature, *J. Power Sources*, 267(2014), p. 69.
[109] C.M. Stander, Kinetics of formation of magnesium hydride from magnesium and hydrogen, *Z. Phys. Chem.*, 104(1977), No. 4-6, p. 229.
[110] M.H. Mintz, Z. Gavra, and Z. Hadari, Kinetic study of the reaction between hydrogen and magnesium, catalyzed by addition of indium, *J. Inorg. Nucl. Chem.*, 40(1978), No. 5, p. 765.
[111] S. Shriniwasan, H.Y. Tien, M. Tanniru, F. Ebrahimi, and S.S.V. Tatiparti, Transition from interfacial to diffusional growth during hydrogenation of Mg, *Mater. Lett.*, 161(2015), p. 271.
[112] P. Trivedi and K.C. Nune, Bioactivity, cytocompatibility and effect of cells on degradation behavior of Mg–2Zn–2Gd alloy, *Nanomater. Energy*, 8(2019), No. 2, p. 117.
[113] T.C. Xie, H. Shi, H.B. Wang, Q. Luo, Q. Li, and K.C. Chou, Thermodynamic prediction of thermal diffusivity and thermal conductivity in Mg–Zn–La/Ce system, *J. Mater. Sci. Technol.*, 97(2022), p. 147.
[114] Y. Li, Q.F. Gu, Q. Li, and T.F. Zhang, *In-situ* synchrotron X-ray diffraction investigation on hydrogen-induced decomposition of long period stacking ordered structure in Mg-Ni-Y system, *Scripta Mater.*, 127(2017), p. 102.
[115] G. Liang, Synthesis and hydrogen storage properties of Mg-based alloys, *J. Alloys Compd.*, 370(2004), No. 1-2, p. 123.
[116] H. Yong, S.H. Guo, Z.M. Yuan, Y. Qi, D.L. Zhao, and Y.H. Zhang, Improved hydrogen storage kinetics and thermodynamics of RE−Mg-based alloy by co-doping Ce−Y, *Int. J. Hydrogen Energy*, 44(2019), No. 31, p. 16765.
[117] K.B. Wu, Q. Luo, S.L. Chen, Q.F. Gu, K.C. Chou, X.L. Wang, and Q. Li, Phase equilibria of Ce−Mg−Ni ternary system at 673 K and hydrogen storage properties of selected alloy, *Int. J. Hydrogen Energy*, 41(2016), No. 3, p. 1725.
[118] D. Khan, J.X. Zou, X.Q. Zeng, and W.J. Ding, Hydrogen storage properties of nanocrystalline $Mg_2Ni$ prepared from compressed $2MgH_2$−Ni powder, *Int. J. Hydrogen Energy*, 43(2018), No. 49, p. 22391.
[119] M.H. Li, Y.F. Zhu, C. Yang, J.G. Zhang, W. Chen, and L.Q. Li, Enhanced electrochemical hydrogen storage properties of $Mg_2NiH_4$ by coating with nano-nickel, *Int. J. Hydrogen Energy*, 40(2015), No. 40, p. 13949.
[120] T. Kohno, S. Tsuruta, and M. Kanda, The hydrogen storage properties of new $Mg_2Ni$ alloy, *J. Electrochem. Soc.*, 143(1996), No. 9, p. L198.
[121] J.S. Han and J.Y. Lee, A study of the hydriding kinetics of $Mg_2Ni$, *J. Less Common Met.*, 131(1987), No. 1-2, p. 109.
[122] L.Q. Li, I. Saita, K. Saito, and T. Akiyama, Effect of synthesis temperature on the hydriding behaviors of Mg−Ni−Cu ternary hydrogen storage alloys synthesized by hydriding combustion synthesis, *J. Alloys Compd.*, 372(2004), No. 1-2, p. 218.
[123] H.J. Lin, C. Zhang, H. Wang, L.Z. Ouyang, Y.F. Zhu, L.Q. Li, W.H. Wang, and M. Zhu, Controlling nanocrystallization and hydrogen storage property of Mg-based amorphous alloy via a gas-solid reaction, *J. Alloys Compd.*, 685(2016), p. 272.
[124] J.J. Jiang, H.Y. Leng, J. Meng, K.C. Chou, and Q. Li, Hydrogen storage characterization of $Mg_{17}Ni_{1.5}Ce_{0.5}$/5 wt.% Graphite synthesized by mechanical milling and subsequent microwave sintering, *Int. J. Energy Res.*, 37(2013), No. 7, p. 726.
[125] Z.Y. Lu, H.J. Yu, X. Lu, M.C. Song, F.Y. Wu, J.G. Zheng, Z.F. Yuan, and L.T. Zhang, Two-dimensional vanadium nanosheets as a remarkably effective catalyst for hydrogen storage in $MgH_2$, *Rare Met.*, 40(2021), No. 11, p. 3195.
[126] Z.Q. Lan, L. Zeng, G. Jiong, X. Huang, H.Z. Liu, N. Hua, and J. Guo, Synthetical catalysis of nickel and graphene on enhanced hydrogen storage properties of magnesium, *Int. J. Hydrogen Energy*, 44(2019), No. 45, p. 24849.
[127] G. Liang, J. Huot, S. Boily, A. Van Neste, and R. Schulz, Hydrogen storage in mechanically milled Mg−$LaNi_5$ and $MgH_2$−$LaNi_5$ composites, *J. Alloys Compd.*, 297(2000), No. 1-2, p. 261.
[128] M. Ismail, Y. Zhao, X.B. Yu, and S.X. Dou, Improved hydrogen storage performance of $MgH_2$−$NaAlH_4$ composite by addition of $TiF_3$, *Int. J. Hydrogen Energy*, 37(2012), No. 10, p. 8395.